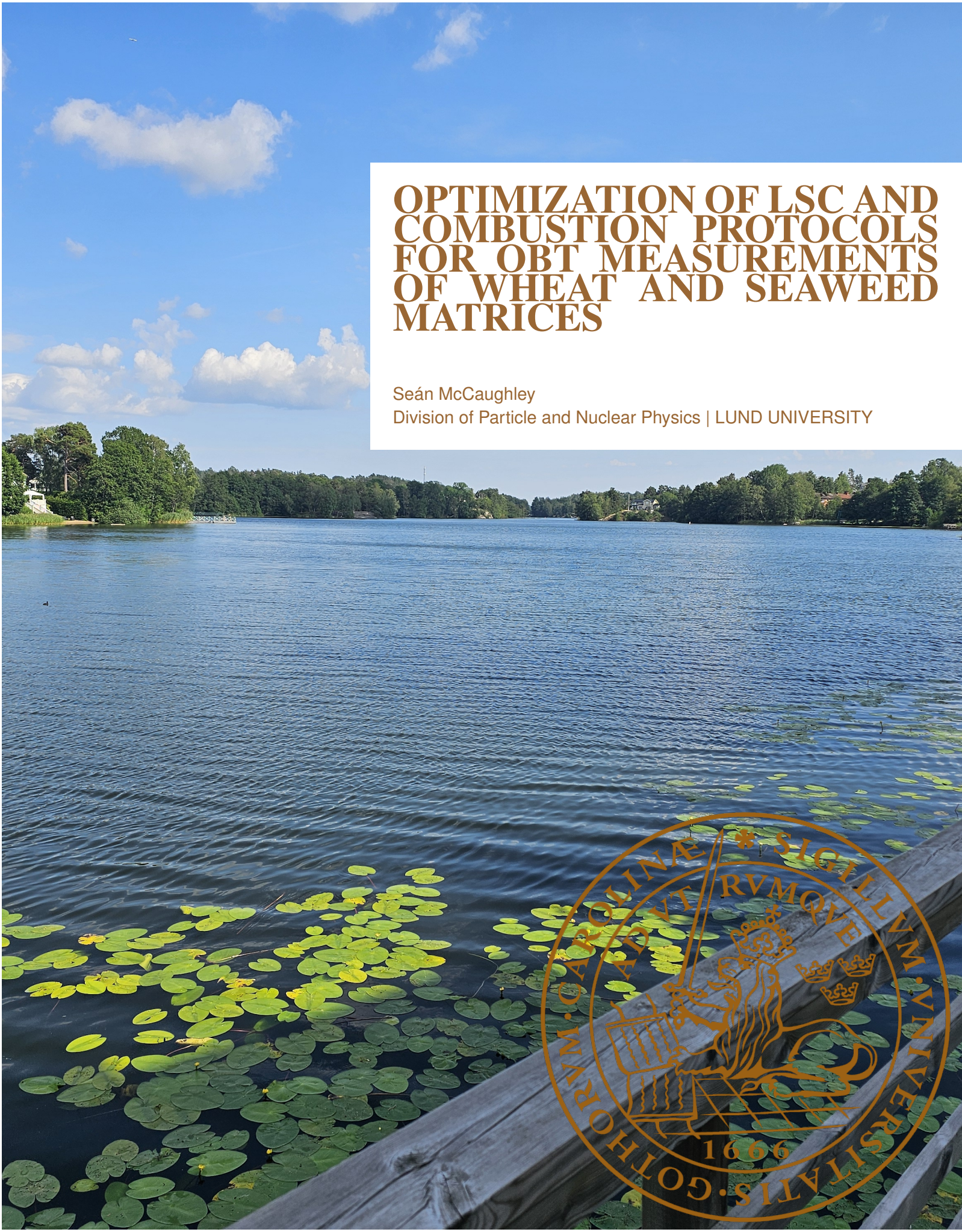

# OPTIMIZATION OF LSC AND COMBUSTION PROTOCOLS FOR OBT MEASUREMENTS OF WHEAT AND SEAWEED MATRICES

Seán McCaughley
Division of Particle and Nuclear Physics | LUND UNIVERSITY


LUND
UNIVERSITY

**Division of Particle and Nuclear Physics**

# OPTIMIZATION OF LSC AND COMBUSTION PROTOCOLS FOR OBT MEASUREMENTS OF WHEAT AND SEAWEED MATRICES

Author: Seán McCaughley

Degree: Masters

1 year (60hp)

Supervisors: Guillaume Pédehontaa-Hiaa, Charlotta Nilsson, Kristina Eriksson Stenström

Date of Examination: June/2026

## Abstract

This project involved the testing and establishment of a base combustion procedure for the newly acquired Raddec Gen IV PYROLYSER and focused on the optimization and correction of the laboratory's previous liquid scintillation counting (LSC) procedure using the Hidex 300 SL.

The pyrolyser was verified to be operational and achieve satisfactory and consistent recoveries across the 6 combustion tubes. A custom organic combustion template was created to process masses of $8\,\mathrm{g}$ to $19\,\mathrm{g}$ of seaweed (*Fucus serratus* and *Fucus vesiculosus*) and wheat-like samples. Recovery rates of $(85\pm8)\,\%$ to $(100\pm10)\,\%$ and $(88\pm1)\,\%$ to $(94\pm1)\,\%$ were achieved for seaweed and wheat, respectively. The combustion water yield was increased by $2$ to $4$ times compared to that of the default organic combustion template from the manufacturer. Furthermore, a post-combustion sample cleaning procedure was introduced and assessed in order to lower the quench of the combustion water.

Technical corrections to the Hidex 300 SL included refinements to the Triple-to-Double Coincidence Ratio (TDCR) calculations and the rectification of the uncertainty estimation logic. Experimental validation confirmed that the manufacturer's default coincidence time of $35\,\mathrm{ns}$ is the optimal value for this system. The optimized Region of Interest (ROI) was determined to be channel numbers $20$ to $195$. A well-characterized background model was developed, resulting in a $25\,\%$ decrease in the Minimum Detectable Activity (MDA) for relevant samples. Additionally, accounting for the covariance between double and triple coincidences resulted in a $(21 \pm 2)\,\%$ decrease in the activity uncertainty.

To automate data quality control, a custom data cleaning pipeline was introduced utilizing quartile filtering, z-score progression, and a custom signs test to identify outliers. This methodology resulted in the rejection of $5.1\,\%$ of measurement repetitions and a mean activity reduction of $(34 \pm 27)\,\%$, for affected samples. These functionalities were integrated into a custom-built PySide 6 application, providing post-measurement parameter alteration, custom outlier selection, and interactive visualization of the cleaning process.

# Acknowledgements

First, I would like to thank Guillaume Pédehontaa Hiaa for his continued guidance throughout this project. His expertise with the LSC and his thorough reading and corrections during the writing process were invaluable to the success of this work.

I would also like to thank Charlotta Nilsson for her insightful guidance and corrections during the drafting of this thesis, and Kristina Eriksson Stenström for introducing me to this project and providing steadfast support throughout.

I am grateful to Lund University for the opportunities provided over the past five years as I progressed from a Bachelor's to a Master's student.

ChatGBT and Gemini were used to correct spelling and grammar along with providing assistance for tge creation of the code used for analysis, the PySide 6 application, and for figures in this thesis.

Finally, I would like to thank my family and especially my mother. Without their unwavering support and encouragement, I would not have had the opportunity to reach this stage in my education; they have truly helped me push through the challenges of this journey.

# Contents

# List of Acronyms

| | |
|---|---|
| **AQL** | Activity Quantification Limit |
| **CPM** | Counts Per Minute |
| **DPM** | Disintegrations Per Minute |
| **E-OBT** | Exchangeable-Organically Bound Tritium |
| **FOM** | Figure Of Merit |
| **IQR** | Interquartile Range |
| **LOD** | Limit Of Detection |
| **LSC** | Liquid Scintillation Counting |
| **MCF** | Mass Conversion Factor |
| **MDA** | Minimum Detectable Activity |
| **NE-OBT** | Non-Exchangeable Organically Bound Tritium |
| **OBT** | Organically Bound Tritium |
| **PMT** | Photomultiplier Tube |
| **QIP** | Quench Indicating Parameter |
| **ROI** | Region Of Interest |
| **TDCR** | Triple-To-Double Coincidence Ratio |
| **TFWT** | Tissue Free Water Tritium |

# Introduction

Tritium ($^3$H) is the heaviest naturally occurring isotope of hydrogen, with a name originating from the three nucleons constituting its nucleus. As a low-energy beta emitter with a half-life of $(12.32 \pm 0.02)$ years, its environmental behavior is primarily dictated by its integration into the global water cycle (Eyrolle et al. 2018). Tritium is produced naturally in the atmosphere when galactic cosmogenic radiation creates a neutron flux, leading to the neutron activation of nitrogen ($^{14}$N) and, to a lesser extent, oxygen. While small contributions arise from direct solar accretion and neutron activation of surface lithium, tritium is most commonly found in the environment as tritiated water (HTO), followed by tritiated molecular hydrogen (HT) (IAEA 2025).

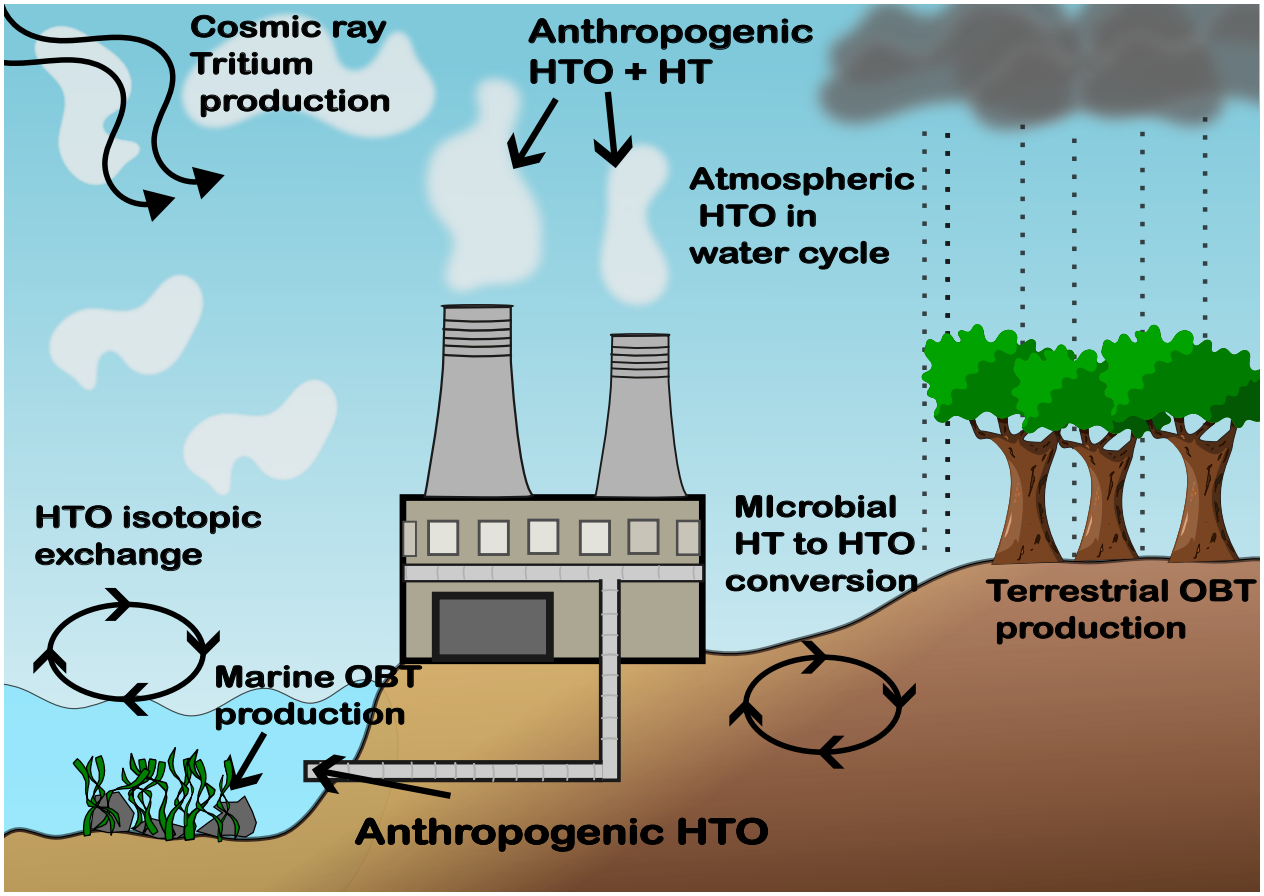


Figure 1.1: Production and life cycle of tritium in the biosphere and atmosphere.

HTO in a liquid and gaseous state readily assimilates into the water cycle and finds equilibrium

with the local environment, as illustrated in Figure 1.1. Before gaseous HT can be assimilated, it must be converted to HTO; while a small amount is oxidized in the atmosphere, the majority is converted by microbial action in soils (IAEA 2025). In recent years, Organically Bound Tritium (OBT) has become of significant interest. OBT is produced in plants when environmental HTO participates in photosynthesis, creating tritiated glucose. Further pathways include metabolic reactions in the plant. Humans can also produce OBT by metabolic reactions, where an estimated $0.5\,\%$ to $3\,\%$ of HTO is converted to OBT (Paquet et al. 2016). The absorption of ingested OBT by humans depends on the organic compounds (Paquet et al. 2016). Approximately $9\,\%$ to $45\,\%$ is incorporated as OBT and the remainder converted to HTO (ICRP 1990). Approximately 9 times more OBT is present in tissues following the ingestion of OBT, compared to HTO ingestion (ICRP 1990).

While OBT levels in a stable environment generally reflect environmental HTO levels, biota ingesting OBT from anthropogenic sources can exhibit significantly elevated concentrations. For example, in the Irish Sea near Cardiff Bay, local flounder and mussels showed OBT concentrations thousands of times higher than ambient HTO levels (G. J. Hunt et al. 2010). Similarly, in Sellafield, plaice and mussels exhibited enhancements of up to 10 times, likely due to the accumulation and ingestion of OBT sources (G. J. Hunt et al. 2010). Furthermore, filter feeders in the Mediterranean Sea far from river mouths carrying HTO have shown OBT levels $3$ to $10$ times higher than that of local HTO levels (Eyrolle et al. 2018). These observations are attributed to the consumption of phytoplankton originating from tritiated zones, demonstrating that OBT can serve as a long-term record of environmental exposure.

The biological impact of tritium is relatively low due to its short beta-particle path length, and environmental baseline levels are typically three to four orders of magnitude below the World Health Organization guidance level for HTO in drinking water of $10\,000\,\mathrm{Bq\,L^{-1}}$ (World Health Organization 2017). However, the global inventory was fundamentally altered between 1952 and 1980 by atmospheric thermonuclear testing. It is estimated that $520\,\mathrm{kg}$ to $664\,\mathrm{kg}$ (IAEA 2025) of tritium was released during this period, dwarfing the natural steady-state production of $220\,\mathrm{g}$ to $330\,\mathrm{g}$ annually (IAEA 2025). This massive anthropogenic influx turned tritium into a proficient tracer for monitoring ocean dynamics and hydrological residence times.

Further anthropogenic sources include industrial processing, nuclear fuel reprocessing, and nuclear fission. Tritium is produced in fission reactions via ternary decay paths and the neutron activation of lithium and boron in reactor coolants. While light water reactors are common, heavy water reactors produce 20 times more tritium due to neutron activation of the deuterium moderator (IAEA 2025). Additionally, tritium is a promising fuel source for future fusion reactions. If fusion becomes a viable power source, established environmental monitoring programs will be vital for assessing the effects of releases from such facilities.

$$^{2}\mathrm{H} +^{3}\mathrm{H} \rightarrow^{4}\mathrm{He} + n + 17.6\mathrm{MeV}$$

Monitoring environmental tritium near such facilities is critical for regulatory compliance and leak detection. Lund University has monitored tritium in the urine of the public following the commissioning of the European Spallation Source (ESS) (Pédehontaa-Hiaa et al. 2020), alongside HTO levels in local water. This project seeks to facilitate the expansion of these surveillance efforts to include OBT analysis of biota in the vicinity of the ESS and the Ringhals nuclear power plant. Ringhals currently presents a dynamic monitoring environment; while reactors R1 and R2

are currently being dismantled, reactors R3 and R4 remain operational (1081 MWe and 1134 MWe, respectively), with all four reactors scheduled for environmental releases over the coming years.

Proper extraction of OBT entails unique challenges compared to HTO processing. The standard approach involves the combustion and oxidation of a dried sample, where the resulting combustion water is measured via liquid scintillation counting (LSC) (IAEA 2025). Complete combustion is required to prevent any possible isotopic fractionation between hydrogen species due to differing masses. Furthermore, maximizing water yield is essential for efficient experimental throughput and increased measurement volumes.

The interest to measure OBT increased during the turn of the century. However, there were no standard procedures or widespread reference materiakls to validate a labs experimental method. In 2012 the OBT International group was formed in order to reduce uncertainty of measurements, provide better public dose assessments, and to provide better model validation (N. Baglan, S. Kim, et al. 2013). Since the formation, 7 inter-laboratory comparisons have been conducted, with 7 different reference materials (Zaharov, Nedelcu, and Dupleac 2025).

This project focused on establishing a robust combustion routine for wheat as well as seaweed species (*Fucus serratus* and *Fucus vesiculosus*) using a RADDEC Gen IV tri-zone PYROLYSER. The work aimed to facilitate the complete combustion and to maximize the dried sample mass to be combusted and combustion water yields. Additionally, optimizations were made to the laboratories LSC system protocols, including adjustments to the region of interest (ROI), coincidence windows, measurement times, and the establishment of a well-known background, along with the establishment of a data cleaning routine. The 26 OBT wheat reference material from the 2026 PROCORAD interlaboratory (PROCORAD 2025) was combusted and measured in order to validate the overall measurement procedure.

# Background

## 2.1 Forms and Origins of Tritium in Biota

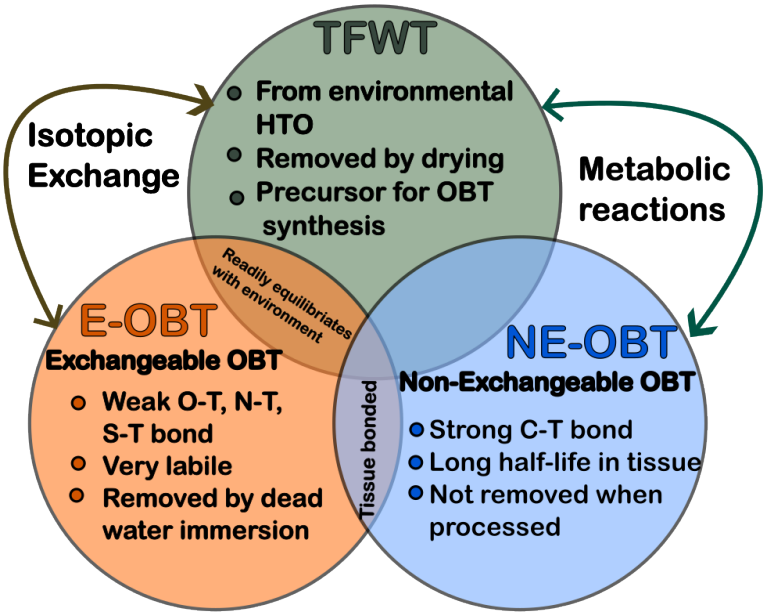


Figure 2.2: A comparison of the different forms of tritium found in biota (inspired by Eyrolle et al. 2018).

Tritium in biological samples occurs primarily in two forms: tissue free water tritium (TFWT) and OBT. TFWT refers to tritium present in the free-water contained within biological tissues, whereas OBT refers to tritium that has been incorporated into organic molecules within the tissue. In humans, TFWT can enter the body through ingestion, inhalation, and absorption through the skin (IAEA 2025). OBT may be introduced through the ingestion of food containing OBT or formed internally through metabolic processes in which a small fraction of TFWT becomes incorporated into organic molecules as described in the introduction. In plants, OBT is primarily formed through metabolic processes such as photosynthesis, resulting in increased incorporation during periods of growth (S. B. Kim et al. 2008).

OBT can be further divided into two categories: exchangeable organically bound tritium (E-OBT) and non-exchangeable organically bound tritium (NE-OBT). The differences are illustrated in Figure 2.2. E-OBT is tritium that is bound to exchangeable hydrogen sites, typically associated

with oxygen, nitrogen, or sulfur atoms in organic molecules. These bonds are relatively labile, allowing isotopic exchange with environmental hydrogen, particularly with the surrounding water molecules. As a result, in a steady-state environment E-OBT is generally in isotopic equilibrium with TFWT (Belot, Roy, and Métivier 1997 as mentioned in Eyrolle et al. 2018).

In contrast, NE-OBT consists of tritium covalently bound to carbon atoms within organic molecules. These bonds are sufficiently stable to prevent isotopic exchange with environmental hydrogen. Consequently, NE-OBT is removed from biological systems primarily through radioactive decay or metabolic turnover. Under long-term steady-state environmental conditions, NE-OBT concentrations tend to reflect the surrounding HTO levels. However, in non-steady-state environments, NE-OBT concentrations may differ significantly from those of TFWT and E-OBT, as NE-OBT reflects earlier environmental conditions at the time of biosynthesis (S. Kim and Korolevych 2013).

This property allows NE-OBT to serve as a historical record of environmental tritium exposure. One promising application of this approach involves the analysis of annually formed tree rings. Tritium that is incorporated into cellulose during ring formation becomes fixed as NE-OBT, enabling reconstruction of environmental tritium concentrations during the year of growth (Love, J. R. Hunt, and Knezovich 2003).

In most studies performing OBT measurements, the quantity determined corresponds primarily to NE-OBT. During sample preparation, E-OBT is generally removed by immersing the sample in tritium-free water (often referred to as "dead water") (F. Pointurier et al. 2003, Kuwata et al. 2025). This allows labile hydrogen atoms within the organic material to equilibrate with the surrounding water. Because the quantity of hydrogen in the tritium-free water is orders of magnitude greater than that present in the sample, isotopic exchange effectively replaces all tritium at labile sites with protium, resulting in the removal of E-OBT prior to analysis.

## 2.2 Combustion

As established in Section 2.1, the analysis of NE-OBT requires the total removal of TFWT and E-OBT. While TFWT is readily removed by drying the sample via oven or freeze-drying (IAEA 2025), the extraction of NE-OBT from its covalent bonds necessitate another approach. To liberate the hydrogen from these organic matrices, the sample must undergo controlled and complete combustion, converting the biological material into measurable HTO and carbon dioxide, while preventing fractionation. The efficiency of the combustion process is determined by the recovery factor. Recovery factors are commonly determined using one of two approaches: combustion of an OBT reference material with similar matrix composition and a comparison of experimentally measured and known activities (Nayak et al. 2019), or calculation of a water equivalent factor (WEF), representing the expected mass of tritiated water assuming complete hydrogen liberation and oxidation. The recovery factor is then calculated as the ratio of the measured to expected water mass. This study utilized the latter.

The recovery factor $R$, is defined as the ratio of the mass of the recovered water to the expected water mass:

$$R = \frac{m_{rw}}{WEF} \tag{2.1}$$

where $m_{rw}$ is the mass of recovered water.

The WEF converts the hydrogen content of the dried sample into the corresponding mass of water expected following complete liberation and oxidation of hydrogen:

$$WEF = \frac{m_d \cdot n_h}{n_{h_{cw}}} \tag{2.2}$$

where $m_d$ is the mass of the dried sample, $n_h$ is the hydrogen content of the dried sample, and $n_{h_{cw}}$ is the hydrogen content of the combustion water. $n_h$ is determined either experimentally using an elemental analyzer (Chen et al. 2022a, Zaharov 2025) or estimated based on the predominant chemical composition of the sample matrix (F. Pointurier et al. 2003, Krištof, Chipanovska, and Kožar Logar 2023, Lin et al. 2020).
The recovery factor can be restated as,

$$R = \frac{m_{rw} \cdot n_{h_{cw}}}{m_d \cdot n_h} \tag{2.3}$$

The WEF can also be used to estimate the amount of dried sample required to achieve a desired water output, which is particularly important for low-activity samples, where the water volume has an inverse relationship with the minimum detectable activity (Section 2.3.4).

The main factors affecting hydrogen recovery include the heating profile, sample mass, airflow rate, and trapping configuration. The combustion setup used in this thesis is described in Section 3.3.1.
While having good recovery is valuable for experimental throughput, the conversion between activity concentration in $\mathrm{Bq\,L^{-1}}$ ($a$) and $\mathrm{Bq\,kg^{-1}}$ ($A$) is independent of the recovery factor. The activity concentration is converted from the volume of the combustion water to the mass of the dry sample by multiplying with the ratio of the WEF to the dry mass (Crozet et al. 2025,Pointurier, Baglan, and Alanic 2004). By applying Equation 2.2 and 2.3 the conversion only relies upon the ratio of the hydrogen content in the dry mass to the hydrogen content of the combustion water. In this thesis this ratio is called the mass conversion factor (MCF). The derivation is shown in Equation 2.4.

$$A = \frac{a \cdot WEF}{m_d} = \frac{a \cdot m_c w}{R \cdot m_d} = a \cdot \frac{n_h}{n_{h_{cw}}} = a \cdot MCF \tag{2.4}$$

## 2.3 Liquid Scintillation Counting

LSC is a versatile and widely used technique for measuring $\beta$, $\alpha$ and $\gamma$ radiation. LSC is one of the most common measurement technique used for low activity $\beta$ emitters, such as $^{3}$H and $^{14}$C, because of quicker sample preparation times and lower operational cost. However, the often low-activity of environmental samples can push the machine to work close to its limit of detection (LOD). This section will cover the scintillation process, the working principles of LSC, quenching effects and correction methods, and finally the LOD in LSC measurements.

### 2.3.1 LSC Principles

The scope of this thesis focuses on the utilization of LSC for the detection of low-activity and low-energy $\beta$ emitters. While LSC can be applied for the detection of $\gamma$-rays and $\alpha$ particles, the following sections will narrow the discussion for $\beta$ radiation.

#### 2.3.1.1 Liquid Scintillation

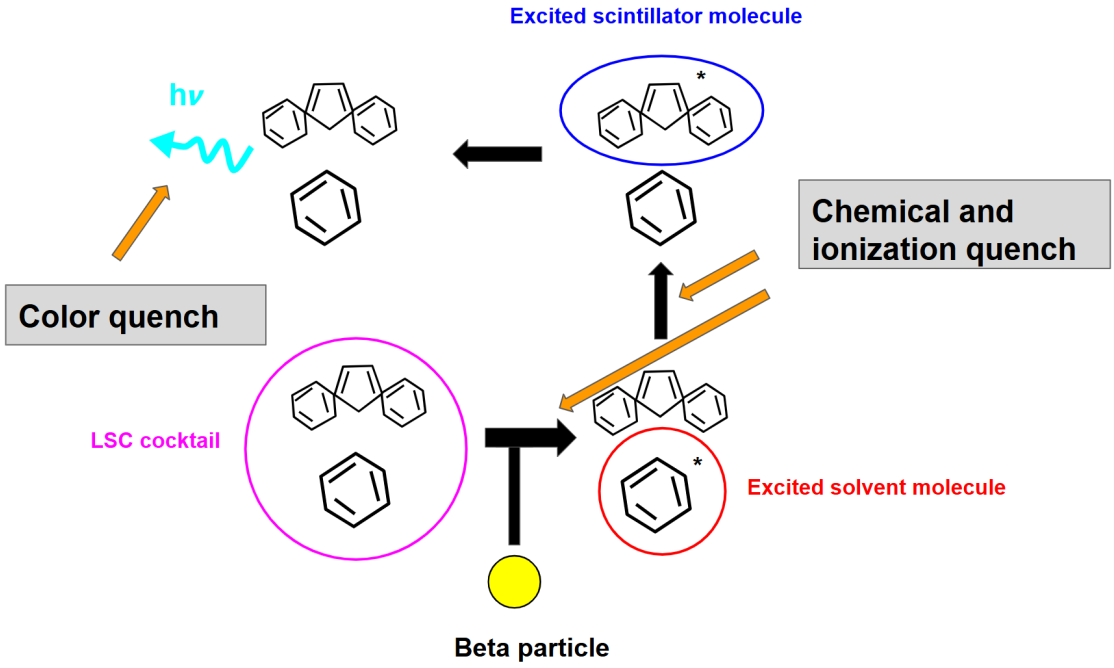


Figure 2.3: Schematic of the scintillation process in liquid scintillation counting (Inspired by Schubert and Kallmeyer 2023).

$\beta$ particles have a short energy deposition range. This short range requires the scintillator to be in close proximity to the $\beta$ emitter. As a result aqueous samples are directly mixed with a liquid cocktail containing the scintillator.
The earliest reports of aromatic compounds exhibiting scintillation properties were published by Herforth and Kallmann 1949. Aromatic compounds continue to serve as the primary basis of modern scintillation cocktails. These cocktails consist of a scintillator dissolved in an appropriate solvent. Emulsifiers are added if mixing with an aqueous medium is required, as is the case in this thesis.

The scintillation process is illustrated in Figure 2.3. A decay event produces a $\beta$ particle with a characteristic kinetic energy. Because there are far more solvent molecules than scintillator molecules, the $\beta$ particle will predominantly undergo inelastic scattering with the solvent, depositing part of its energy. The excited solvent molecule then transfers this energy to a scintillator molecule, which subsequently de-excites and emits a photon in the 375–400 nm wavelength range (L'Annunziata and Kessler 2012). This process may repeat multiple times until the $\beta$ particle has lost all of its

kinetic energy. The emitted photons are then detected by the LSC instrument, as described in the following section.

### 2.3.2 LSC Working Principle and Features

LSC instruments are designed to detect and quantify the scintillation photons produced during the scintillation process described in Section 2.3.1.1. Modern LSC instruments are typically either double or triple coincidence counters. Double coincidence counters only record an event if both detectors are triggered within a specified coincidence window. Popular commercial double coincidence counters include the PerkInElmer Quantulus 1220 (NPL 2006) and the PerkInElmer Tri-Carb 2810TR (University of Saskatchewan n.d.).

Triple coincidence counters, on the other hand, track both double and triple coincidences, allowing for the improved rejection of counts originating from luminescence effects if the machine is operated in triple coincidence mode alone. It also provides a unique method to correct for counting efficiencies, as discussed further in Section 2.3.3.2. The Hidex 300 SL (Hidex Oy 2023) is an example of a triple coincidence counter and is the instrument used in this thesis. Further discussion on the specific characteristics of this machine can be found in Section 3.2.2.

This section will detail the general operational principles of an LSC instrument.

#### 2.3.2.1 LSC Components

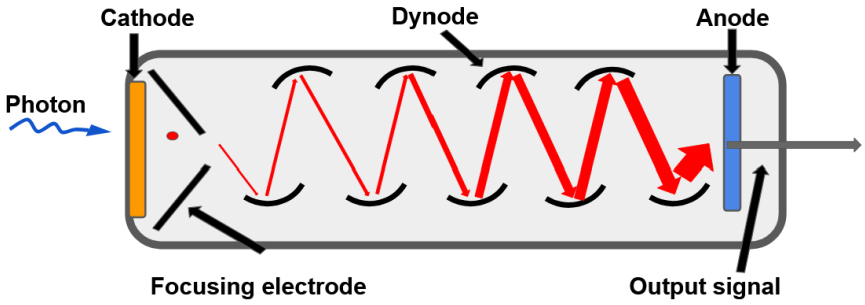


Figure 2.4: Schematic of a PMT. The width of the arrows represent the number of electrons.

A typical LSC instrument consists of several key components: a sample tray, photomultiplier tubes (PMTs), signal processing electronics, and shielding. The tray holds multiple samples, and an automated arm transfers each vial into the measurement position. The PMT's are arranged around the sample to provide approximately $2\pi$ optical coverage. Passive shielding by lead and copper is standard along with active shielding by an external guard detector.

The PMTs are highly sensitive light detectors that convert scintillation photons into electrical signals (Figure 2.4). When a photon strikes the photocathode, it ejects an electron via the photoelectric effect. This electron is accelerated through a series of dynodes, each producing an avalanche of secondary electrons that amplifies the initial signal by a factor $> 10^6$ (L'Annunziata and Kessler 2012). The resulting pulse is then processed by the LSC system's electronics to determine its amplitude

and timing. The pulse amplitude is proportional to the number of detected photons, which corresponds to the energy of the $\beta$-particle that produced the scintillation event.
Each decay event emits multiple scintillation photons in random directions. To register an event, photons must be detected within a defined coincidence window by two or more PMT's; single-photon background events are therefore rejected. For valid coincidences, the signals are summed and assigned a digital channel number. Each channel number corresponds to a narrow pulse-height window, and an event is counted in the channel number whose window matches the measured pulse height.

For $\beta$-particle measurements, the user defines a ROI within the spectrum. The counts within this ROI are summed and corrected for dead time. A double coincidence counter returns one value. A triple coincidence counter can return 5, the three values from the double coincidence spectra, the value from the combined double coincidence spectrum and the value from the triple coincidence spectrum.

#### 2.3.2.2 Background

Background in LSC measurements originates from several sources, including cosmic radiation, luminescence, statics and other radiation sources in the sample (L'Annunziata and Kessler 2012). Cosmic rays are mitigated by passive and active shielding. Chemical and photo luminescence originate from the interaction of ambient light and chemical reactions with the scintillation cocktail, respectively. These effects can be minimized by 24 hours of dark exposure prior to measurement (Ohki et al. 2021) along with temperature control. Statics are small electrical charges that accumulate on the surface of the scintillation vial, which can produce pulses in the PMT. Use of anti-static gloves along with repeated short measurements can reduce the impact of statics. Modern LSC instruments are equipped with anti-static features. Other radiation sources in the sample, can be limited by proper sample preparation techniques, such as chemical separation or purification.

### 2.3.3 Quenching and Quench Correction

Figure 2.3 also points to junctions in the scintillation process where a phenomenon known as quenching can occur. Quenching refers to any process or property that prevents the efficient conversion of the $\beta$ particles energy into detectable photons, in the context of LSC. There are four main types of quenching: physical quenching, ionization quenching, chemical quenching, and color quenching (L'Annunziata and Kessler 2012, Schubert and Kallmeyer 2023). The correction of quenching effects is essential for accurate activity measurements, especially at low activity levels. Limiting quenching effects improves the detection efficiency of the LSC instrument, which in turn lowers the LOD.

#### 2.3.3.1 Quenching Effects

**Physical quenching:** occurs when the energy deposited by the $\beta$ particle cannot be efficiently transferred to the scintillator. The most common cause of physical quenching is phase separation between the sample and the scintillation cocktail. This underscores the importance of maintaining

a homogeneous mixture. Selecting an appropriate scintillation cocktail and using a sample-to-cocktail ratio that ensures sufficient miscibility are both essential for minimizing the effects of physical quenching. The optimal sample-to-cocktail ratio typically falls between 8mL/12ml and 10ml/10ml, depending on the specific cocktail used (Pujol and Sanchez-Cabeza 1999, Arun, Vijayalakshmi, et al. 2019).

**Ionization quenching:** is a process that primarily affects low-energy $\beta$ emitters, such as tritium (Carles et al. 2004). The relationship between the energy supplied by the $\beta$ particle and the light output from scintillation event is nonlinear, and this nonlinearity depends on the linear energy transfer (LET) of the $\beta$ particle (L'Annunziata and Kessler 2012).

Low-energy $\beta$ particles have large LET values, meaning they deposit their energy over a short distance. This creates a high density of excited solvent molecules in a small volume of the scintillation cocktail. At such high densities, excited solvent molecules are more likely to interact with one another. One molecule can transfer its energy to another already-excited molecule, forming a so-called super-excited molecule. These super-excited molecules preferentially de-excite via ionization rather than transferring energy to the scintillator, reducing the light output (L'Annunziata and Kessler 2012). Unlike the other types of quenching, ionization quenching cannot be mitigated by sample preparation techniques. Instead, it must be corrected for during data analysis.

**Chemical quenching:** is caused by the presence of chemical substances that interfere with the energy transfer process between the solvent and the scintillator. This can happen either by directly absorbing the energy or by interacting with the excited solvent or scintillator molecules, thereby preventing photon emission. In environmental HTO or OBT samples, chemical quenching is typically caused by organic contaminants or impurities in the water. Chemical quenching can be minimized by proper sample preparation, such as filtration or purification of the sample prior to mixing with the scintillation cocktail, as detailed in *Standard Methods FOR THE Examination of Water and Wastewater 20th Edition* 1998.

**Color quenching:** differs from the other quenching mechanisms in that it does not interfere with the scintillation process itself. Instead, it reduces the number of scintillation photons that reach the PMTs of the LSC system. This occurs when colored compounds present in the sample absorb part of the emitted light, thereby lowering the detected count rate. Color quenching can be effectively minimized by ensuring that samples are clear and colorless prior to measurement. In practice, this is commonly achieved through chemical neutralization, purification steps, and subsequent distillation, which remove or degrade colored substances (Farrow et al. 2017).

#### 2.3.3.2 Quench Correction

The LSC instrument reports the counts per minute (CPM) detected within predefined ROI. However, because of the various quenching effects discussed earlier, the measured CPM cannot be directly related to the disintegrations per minute (DPM) of the radionuclide. To do so, one must determine the detection efficiency ($\epsilon$), and apply Equation 2.5. The efficiency is directly related to the total quench of a sample and can be obtained through quench-indicating parameters (QIPs)

(L'Annunziata and Kessler 2012). This is often done by producing a quench correction curve as described later in this section.

$$DPM = \frac{CPM}{\epsilon} \tag{2.5}$$

Once, the DPM is found the activity for a sample with volume V, over a measurement time $t_S$, with mass conversion factor MCF is defined as:

$$A = \frac{DPM \cdot MCF}{60 \cdot t_S \cdot V} \tag{2.6}$$

The mass conversion factor is discussed in Section 2.2.

To understand QIPs, it is first necessary to consider how the degree of quench influences the LSC spectrum. Quenching reduces the number of photons produced per decay event, which lowers the apparent energy of the $\beta$ particle. As a result, the LSC spectrum shifts toward lower channel numbers as quench increases. Quench also decreases the total number of detected events, thereby reducing the overall detection efficiency. An example of this behavior is shown in Figure 2.5, where a known HTO standard was spiked with increasing amounts of nitromethane. Table 2.5 illustrates the corresponding decreases in CPM and efficiency as the concentration of the quenching agent increases.

The effects of quenching are especially pronounced at low $\beta$ energies, such as those of tritium. L'Annunziata and Kessler 2012 performed a similar experiment for $^{14}$C and found that, although the spectra also shifted to lower energies, the total counts and efficiency decreased far slower than in the case of tritium. Their $^{14}$C also achieved efficiencies in the high ninety-percent range, whereas the maximum efficiency they obtained for tritium was approximately $60\,\%$, highlighting the strong impact of ionization quench at low energies.

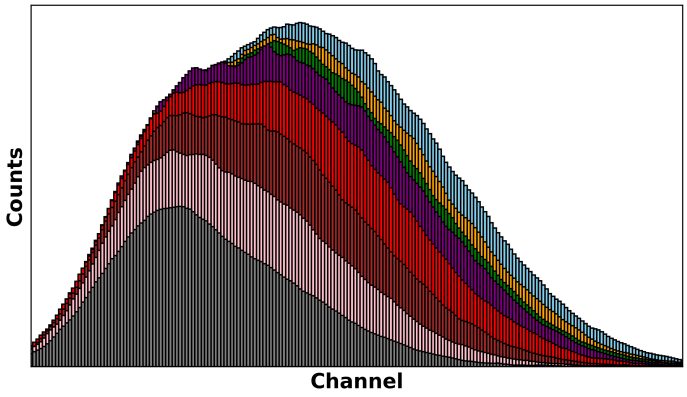


| Nitromethane (µL) | $\epsilon$ (%) | CPM |
|---|---|---|
| 0 | 32.49 | 36612 |
| 5 | 31.09 | 34524 |
| 10 | 29.47 | 33000 |
| 15 | 28.35 | 32112 |
| 26 | 25.54 | 28524 |
| 45 | 20.26 | 22932 |
| 70 | 15.30 | 17148 |
| 110 | 9.94 | 10740 |

Figure 2.5: (Left) LSC spectra of an HTO standard spiked with increasing quantities of nitromethane. (Right) Affects of increasing quench levels on detection efficiency and CPM for an HTO standard.

**External standards** There are several procedures for performing quench corrections, each using its own QIP. The choice of QIP is typically determined by the specifications of the LSC instrument. Methods such as the Spectral Quench Parameter SQP(e) and the Transformed Spectral Index tSIE are used in the Quantulus 1220 (Jakonić et al. 2014) and the Tri-Carb (Arun, Vijayalakshmi, et al. 2019) LSC instruments, respectively. Both methods determine the QIP from the position of the Compton edge, which shifts to lower channel numbers with increasing quench.

These methods fall into the general class of external-standard quench correction techniques, in which an additional radiation source commonly $^{226}$Ra or $^{152}$Eu (L'Annunziata and Kessler 2012) is used to generate the QIP. The emitted $\gamma$-rays interact with the sample to produce Compton electrons, which initiate the scintillation process as described in Section 2.3.1.1. A key advantage of external-standard methods is that the QIP is derived from the highly-active external source rather than from the sample itself. This is particularly beneficial for low-activity samples, where the sample count rates are relative to the background levels.

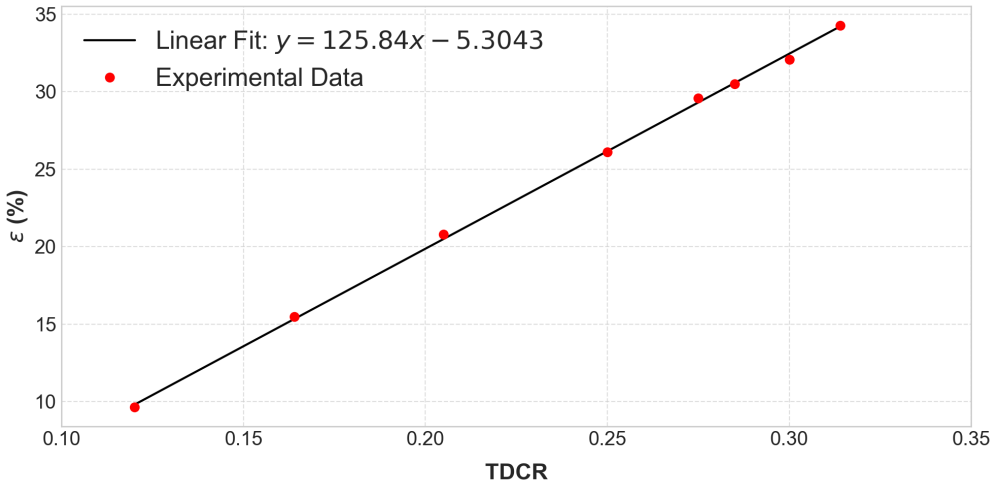


Figure 2.6: TDCR quench correction curve for HTO standards measured with the Hidex 300 SL. The measured TDCR values are plotted against the corresponding detection efficiencies. A linear fit was applied over the quench range.

The Hidex 300 SL used in this project employs the Triple-to-Double Coincidence Ratio (TDCR) method, which uses an internal QIP generated solely from the scintillation light of the sample. The TDCR is found by dividing the total triple to double coincidence counts in a defined ROI. TDCR values can be used in two ways to perform quench correction. The first, recommended by Hidex, involves generating a TDCR-based quench correction curve, analogous to SQP(e) or tSIE curves (Arun, Viswanathan, et al. 2021; Nayak et al. 2019). The second approach combines the experimentally measured TDCR value with theoretical calculations of detection statistics to determine the detection efficiency directly (Arun, Viswanathan, et al. 2021; Lecompte et al. 2020). A formal derivation of the theoretical TDCR and a detailed explanation of its practical application are provided in Appendix A

The TDCR correction curve relates the measured TDCR value to the corresponding detection efficiency. It is constructed by measuring a series of standards of known activity with systematically

varied quench levels. To ensure accurate quench correction, the standards must contain the same radionuclide as the unknown samples. Quench levels are adjusted by adding controlled amounts of the quenching agent (Ex: nitromethane). Figure 2.6 shows an example of a TDCR correction curve for an HTO standards that was previously established by the laboratory. This thesis uses the pre-established curve for efficiency corrections. The adopted TDCR model used to determine the detection efficiency is linear.

### 2.3.4 Limits of Detection

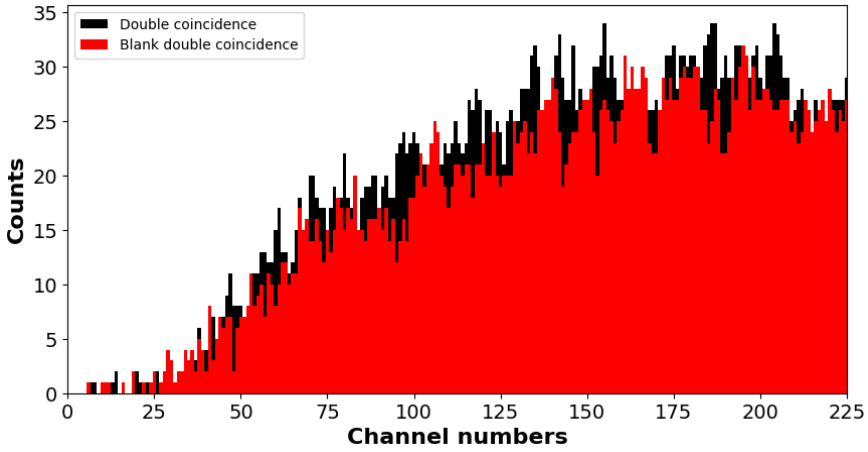


Figure 2.7: Comparison of sample and background spectra for a $3\,\mathrm{Bq\,L^{-1}}$ HTO standard.

Environmental samples often contain radioactivity at levels close to the LOD of an LSC instrument. An example of the subtle differences between sample and background spectra is shown in Figure 2.7. To confidently report such low-level measurements, LOD of the LSC instrument and the corresponding minimum detectable activity (MDA) of the sample must be established. These quantities are determined using Currie statistics (Currie 1968).

The Currie formulation of the detection limit is defined relative to the 'critical level' ($L_C$). The value of $L_C$ defines a binary decision threshold: measurements above $L_C$ are considered detected, and those below it are not. $L_C$ is determined from the probability distribution of the background, which is assumed to follow a normal distribution, as illustrated in Figure 2.8. The level is typically set such that only a small fraction $\alpha = 5\,\%$ of background measurements would exceed $L_C$ (Currie 1968).
The detection limit ($L_D$) is defined such that only a small fraction of the gross signal (typically $\beta = 5\,\%$) is below the critical level. The gross signal is also assumed to have a normal distribution. Mathematically the critical level and detection limit are formulated as:

$$L_C = k_\alpha \sigma_0 \tag{2.7}$$

$$L_D = L_C + k_\beta \sigma_T \tag{2.8}$$

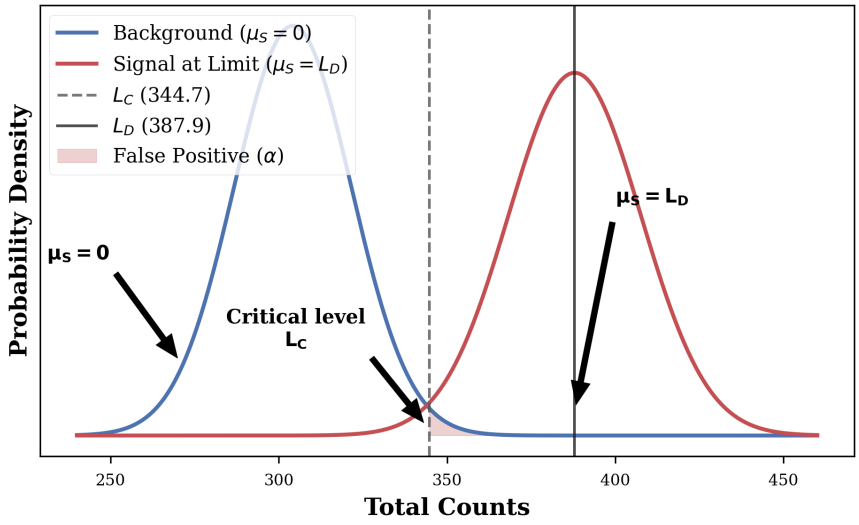


Figure 2.8: Display of the LOD, given a background sample measured 10 times for an hour.

The factors $k_\alpha$ and $k_\beta$ corresponds to the upper and lower z-score for the respective $\alpha$ and $\beta$ values. The parameters $\sigma_0$ corresponds to the uncertainty of the total signal for an average sample count of $\mu_S = 0$. $\sigma_T$ is defined for a radioactive sample using Poisson statistics in Equation 2.9, it is the uncertainty of the total signal with $L_D = \mu_T$.

$$\sigma_T^2 = \sigma_{S+B}^2 + \sigma_B^2 = \mu_S + \mu_B + \mu_B/n \tag{2.9}$$

$\mu_B$ is the mean background counts, n is the number of times a blank has been measured. The LSC instrument operates by finding the samples CPM, which is simply the total counts divided by sample measurement time. Equation 2.9 is reformulated in terms of CPM.

$$\sigma_T = \sqrt{D \cdot t_S + D_{bg} \cdot t_s + D_{bg} \cdot \frac{t_s^2}{t_b}} \tag{2.10}$$

$D$ and $D_{bg}$ are the counts per minute of the sample and background, respectively. $t_S$ and $t_B$ are the measurement times for the sample and background in minutes, respectively. The final term corresponds to the variance of a well-known background that is scaled down to correspond to the time of the sample measurement. Poisson uncertainty scaling is linear.
The two relevant cases (1), a paired observation background ($t_s$=$t_b$), or (2) a well-known background $\sigma_B^2 = 0$ (Currie 1968). The above variance formula is used to compute the critical limit and subsequent LOD by using Equations 2.7 and 2.8, respectively. A 95 % confidence interval is selected, corresponding to $k_\alpha = k_\beta = k = 1.645$. The LOD for a radioactive sample is thus:

$$\text{Paired Observation:} \quad L_D = 2.71 + 4.65\sqrt{D_{bg} \cdot t_s} \tag{2.11a}$$

$$\text{Well-known Blank:} \quad L_D = 2.71 + 3.29\sqrt{D_{bg} \cdot t_s + D_{bg} \cdot \frac{t_s^2}{t_b}} \tag{2.11b}$$

The LOD as defined above, acts as a cutoff point for the minimum amount of CPM of the sample that is considered detected. The MDA is this statement reformulated in terms of the activity of the sample. For a sample volume V, with a detection efficiency $\epsilon$, the MDA ($\mathrm{Bq\,L^{-1}}$ ) is defined as:

$$\text{Paired Observation:} \quad MDA = \frac{2.71 + 4.65\sqrt{D_{bg} \cdot t_S}}{60 \cdot V \cdot \epsilon \cdot t_S} \tag{2.12a}$$

$$\text{Well-known Blank:} \quad MDA = \frac{2.71/t_S + 3.29\sqrt{\frac{D_{bg}}{t_s} + \frac{D_{bg}}{t_b}}}{60 \cdot V \cdot \epsilon} \tag{2.12b}$$

The factor 60 converts from minutes to seconds.

# Equipment and Methods

This chapter discusses the main samples, equipment and methods used in this project. The equipment section provides a brief overview of the primary experimental systems employed, with particular focus on the combustion system, the PYROLYSER GEN IV furnace system (Raddec International 2024), and the liquid scintillation counting system, the Hidex 300 SL (Hidex Oy 2023).

The methods section detail the general operating routines used to process and measure the samples discussed in the following section. This section is divided into three parts: sample collection and preparation, the general combustion routine, and the LSC routine. Optimizations to this base procedure are discussed in the following chapter.

## 3.1 Samples

This section describes the samples processed and measured throughout this project, categorized by type and origin.

- **HTO Standards:** Prepared by spiking tritium-free distilled water with either the 25HTOB PROCORAD HTO standard Yang et al. 2026 or a Revvity tritium internal standard, depending on the target activity concentration.
- **HTO Samples:** Distilled water samples collected from local streams, ponds, and precipitation events.
- **Marine Biota:** Seaweed (*Fucus serratus* and *Fucus vesiculosus*) collected from the Swedish eastern coast.
- **Bulgur:** Commercially available bulgur wheat, used as a proxy for testing grain-based OBT matrices.
- **Wheat OBT Standard:** Provided via the 2026 PROCORAD interlaboratory comparison (PROCORAD 2025). The specific activity was unknown during analysis, with a certified range provided between $10\,\mathrm{Bq\,L^{-1}}$ to $100\,\mathrm{Bq\,L^{-1}}$ of combustion water.

## 3.2 Equipment

### 3.2.1 Pyrolyser

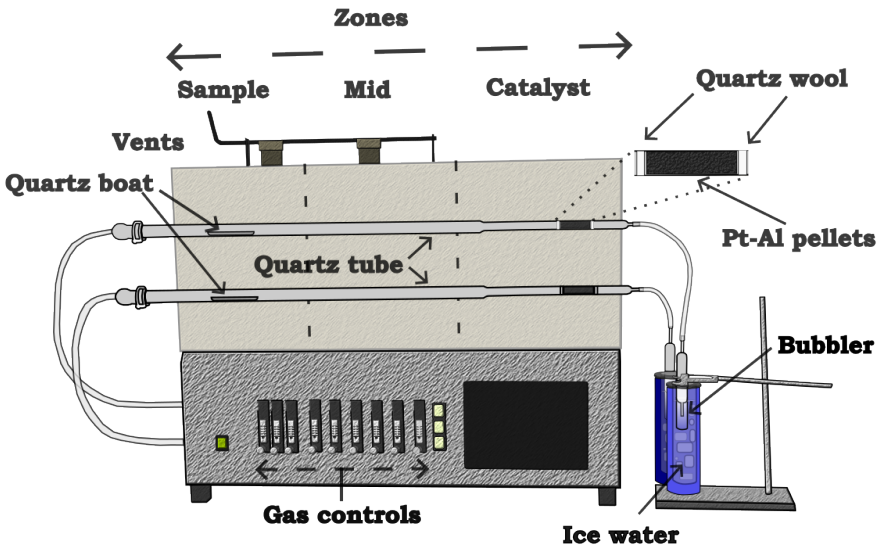


Figure 3.9: A schematic of the combustion setup, showing the Raddec Gen IV PYROLYSER along with the combustion water trap.

Combustion is performed using the Pyrolyser-6 Trio Gen IV (Raddec International 2024). Figure 3.9 displays a schematic of the experimental setup, including the pyrolyser. This 6-tube tubular combustion system features three independently controlled temperature zones: the sample, mid, and catalyst zones, the temperature of each zone can be independently controlled, supporting max temperatures of $950\,^{\circ}\mathrm{C}$.

The sample is housed within a quartz boat located in the sample combustion zone, while the catalyst (Pt-Al) is held between two pieces of quartz wool in the catalyst zone. The mid-zone acts as a buffer between the sample and catalyst zones, preventing the typically higher temperatures of the catalyst zone from leaching into the sample zone.

Six quartz tubes run through all three zones. The pyrolyser supports the supply of air, oxygen, and nitrogen during combustion; these gases can be supplied individually or in combination. Gas flow rates are regulated by the labeled gas controls. During operation, hydrogen and carbon liberated from the sample during combustion are oxidized by the catalyst, with oxygen provided by the compressed air and oxygen supply. The HTO and $CO_2$ are then funneled through silicon tubing to a bubbler trap composed of borosilicate glass. Typically, these combustion products are collected via acid or cold trapping (Croudace, Warwick, and Marsh 2017).

### 3.2.2 LSC

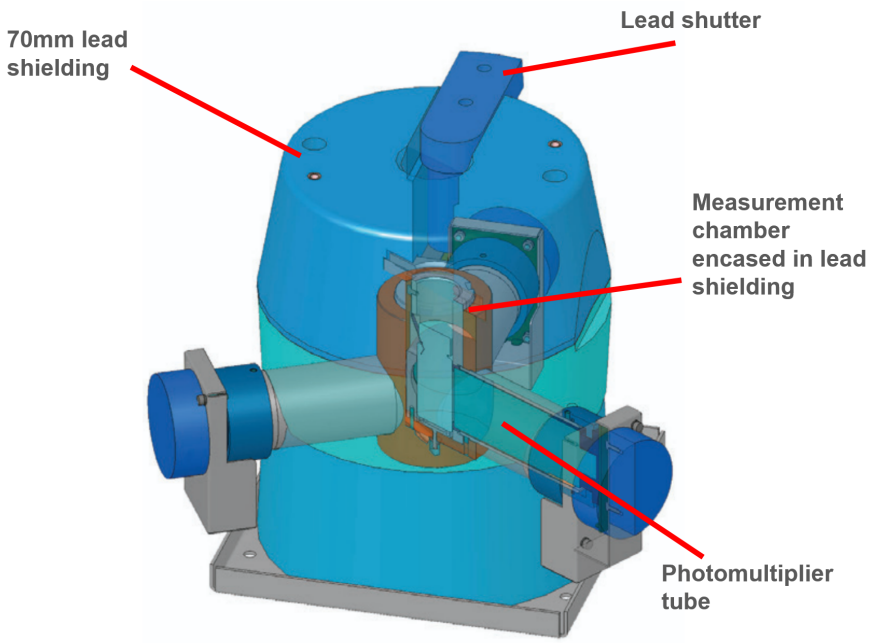


Figure 3.10: Hidex 300 SL liquid scintillation counter used in this project (Adapted from Hidex Oy 2023).

The Hidex 300 SL (Hidex Oy 2023) was utilized for LSC. Samples are placed in a measurement tray and are moved to the measurement chamber by a robotic arm. The measurement chamber is surrounded by the PMT's discussed in Section 2.3.2, allowing for double and triple coincidence detection. The walls of the measurement chamber are coated with a reflective coating, ensuring scintillation light encounters a PMT. An ionizing gun sprays the sample before measurement in the chamber in order to remove electrostatic charges on the vial. The measurement chamber is encased with lead shielding in order to reduce background interference from cosmic rays. A secondary inner layer of copper shielding surrounds the PMT's to capture X-ray emissions from the lead shielding. Measurements are conducted at a stable temperature of 22(2)°C. Energy signals from individual decay events are processed by a multichannel analyzer and assigned to specific channel numbers. The Mikrowin software manages operating conditions and generates the resulting coincidence spectra.

## 3.3 Method

### 3.3.1 Combustion Routine and Sample Preparation

Seaweed species were dried at 70 °C. A grinder was used to homogenize the seaweed samples into a coarse powder, which was then stored in zip-lock plastic bags until combustion preparation. Wheat-like samples such as bulgur and grains were dried at 70 °C prior to combustion.

Dried samples were deposited evenly in a quartz boat and placed in the sample section of the pyrolyser. A combustion routine was applied, with pressurized air and oxygen supplied at different stages at $1\,\mathrm{bar}$. The combustion profile is explained and discussed in Section 4.1.2. The color and pH of the bubbler-trapped combustion water were recorded. The resulting combustion water was stored in polyethylene vials, sealed with parafilm, and refrigerated prior to LSC analysis. Dewar flask containing an ice and salt-water mixture that varied between $0\,^{\circ}\mathrm{C}$ to $-3\,^{\circ}\mathrm{C}$ were used to cool the bubblers. Any gases not trapped were released as exhaust.

### 3.3.2 LSC Routine

Samples are distilled and then stored in plastic jars. Distillation is carried out until all water evaporates to prevent altering the ratio of tritium to protium in the water. The samples are isolated from the environmental atmosphere by wrapping the interface of the lid and jar with parafilm to avoid exchange of water molecules between the water and air. The samples are then stored in a fridge at $4\,^{\circ}\mathrm{C}$ until measurement time.
Measurements are conducted by measuring a sample alongside measuring a blank sample of tritium-free water. $20\,\mathrm{mL}$ polyethylene vials hold the mixed sample and scintillation cocktail (Ultima Gold LLT). A 1/1 ratio of $10\,\mathrm{mL}$ of sample and scintillation cocktail is used, as this ratio has been shown to provide optimal performance for Ultima Gold LLT (Nayak et al. 2019). In the case the sample volume was below $10\,\mathrm{mL}$, the difference was made up by dead water. The same total volumes and ratios of scintillation cocktail to sample were used for making the blanks.
The samples were transferred into the tray of the LSC system and left in the dark for 24 hours to remove chemical and photoluminescence prior to measurement. A custom measurement routine template was specified in the Mikrowin software. The length of the ionizing gun spray and subsequent equilibration time in the measurement chamber prior to measurement were kept consistent at 5 seconds and 20 minutes, respectively.
The coincidence window was investigated over a range of $20\,\mathrm{ns}$ to $55\,\mathrm{ns}$. Individual measurement repetitions were 1 h in duration, while the number of repetitions investigated ranged from 8 to 30. The ROI was evaluated for all possible channel number combinations between 1 and 500. Following optimization, the selected coincidence window, repetition number, and ROI settings were kept constant for subsequent measurements.

Raw spectral data were exported via the default export driver and processed using a bespoke application developed in PySide 6. This application executed a data cleaning pipeline to identify and remove outliers; the specific rejection criteria and the performance of this pipeline are detailed in the Results (Section 4.3.1). For each new LSC measurement tray, a two-sided z-score test was applied to the blank. If the blank measurement was consistent with the well-known background within the combined uncertainty, the well-known background value was used for further calculations. The condition is shown in Equation 3.13.

$$1.645 \geq \left| \frac{D_{WK} - D_{bg}}{\sqrt{\sigma_{WK}^2 + \sigma_{bg}^2}} \right| \tag{3.13}$$

Where $D_{WK}$ and $D_{bg}$ are the CPM of the well-known background and the blank, respectively. $\sigma$ represents the corresponding uncertainties. This calculation is done for both the double and triple

coincidence sample set. If either fail this condition, the blank CPM and corresponding paired observation MDA is used.

Because the number of repetitions may differ between the sample and the background after the cleaning process, average count rates were utilized for all subsequent calculations. The TDCR was determined according to Equation 3.14:

$$\text{TDCR} = \frac{T - T_{bg}}{D - D_{bg}} \tag{3.14}$$

Where $T$ and $D$ are the triple and double coincidence CPM for the sample, and $T_{bg}$, $D_{bg}$ denote the corresponding background values, respectively.

The sample DPM was determined using a linear efficiency model (Equation 3.15), where $k$ and $m$ are the linear-fit parameters used to transform the TDCR into detection efficiency ($\epsilon$).

$$\text{DPM} = \frac{D - D_{bg}}{k\left(\frac{T-T_{bg}}{D-D_{bg}}\right) + m} \tag{3.15}$$

The Hidex 300 SL architecture includes triple-coincidence detections as part of the total double-coincidence detections; therefore, the total double-coincidence counts are dependent upon the triple-coincidence counts (Lecompte et al. 2020). To prevent the inflation of the measurement uncertainty, the model accounts for this non-zero covariance. By exploiting the linearity of covariance, the covariance between the total triple and double coincidences is approximately equal to the variance of the triple coincidences:

$$\text{Cov}(T, D_{total}) = \text{Cov}(T, T + D_{only}) = \text{Var}(T) + \text{Cov}(T, D_{only}) \approx \text{Var}(T) \tag{3.16}$$

The final activity was determined by incorporating independent uncertainty propagation for the DPM, sample volume, and MCF (when converting to $\mathrm{Bq\,kg^{-1}}$). The full covariance-adjusted uncertainty ($\sigma_{DPM}$) was calculated as:

$$\begin{aligned}\sigma_{DPM} = \Bigg[ & (\sigma_D^2 + \sigma_{D_{bg}}^2)\left(\frac{\epsilon + k \cdot \text{TDCR}}{\epsilon^2}\right)^2 + (\sigma_T^2 + \sigma_{T_{bg}}^2)\left(\frac{k}{\epsilon^2}\right)^2 \\ & + \sigma_k^2\left(\frac{T - T_{bg}}{\epsilon^2}\right)^2 + \sigma_m^2\left(\frac{D - D_{bg}}{\epsilon^2}\right)^2 \\ & - 2\left(\frac{k(\epsilon + k \cdot \text{TDCR})}{\epsilon^4}\right)(\sigma_T^2 + \sigma_{T_{bg}}^2)\Bigg]^{1/2}\end{aligned} \tag{3.17}$$

Finally, activities are decay-corrected to the date of sample collection.

# Results and Discussion

This chapter discusses the optimizations made to the combustion routine and measurement routines using the PYROLYSER GEN IV furnace system (Raddec International 2024), and the Hidex 300 SL (Hidex Oy 2023), respectively along with discussing the implementation of a post measurement data analysis routine.

## 4.1 Development of Pyrolyser Measurement Procedure

As the pyrolyser represented a novel addition to the laboratory's analytical suite, the primary objective of this project was the establishment of a foundational protocol for seaweed and glucose-dominant matrices, such as wheat. The seaweed and wheat-like samples used are discussed in Section 3.1. This section details a diagnostic check to ensure that the 6 quartz tubes of the pyrolyser are operating correctly. It also details the mass of dried sample combusted and the accompanying yield, pH, and color of the combustion water, along with detailing the developed organic combustion profile. Furthermore, the development and performance of a post measurement procedure is discussed.

### 4.1.1 Diagnostic Check

The recovery of the pyroyser depends on 4 processes:

1. The liberation of hydrogen from the dry matrix;
2. The transport of water vapor and hydrogen from the sample zone to the catalyst;
3. The catalytic oxidation of hydrogen into water vapor;
4. The trapping efficiency of the custom cryogenic trap.

The transport and the trapping of water vapor was independently tested by evaporating de-ionized water. To control the evaporation rate and to prevent boiling the water was mixed with acid washed sand. The initial Raddec recommended configuration of the quartz tube caused water vapor to condense before reaching the silicon tubing, resulting in a recovery of $(88 \pm 3)\,\%$, with noticeable pools of water left in the quartz tube. By limiting the gap between the end of the quartz tube and the pyrolyser, premature condensation ceased. Recovery rates were $(97.0 \pm 0.5)\,\%$ and notably finishing in half the time of the previous configuration. Therefore, the custom cooling trap and transport rate was determined to operate correctly.

To assess the correct operation of the pyrolyser, the recovery rate of the 6 quartz tubes were compared when combusting $\approx 5\,\mathrm{g}$ of de-ionized water mixed with $\approx 7.4\,\mathrm{g}$ of acid washed sand and when combusting $\approx 8.5\,\mathrm{g}$ of *Fucus serratus*. Recovery is determined by finding the ratio of the combustion water yield to the WEF, as discussed in Section 2.2. The average recovery between the 6 tubes for de-ionized water was $(94.4 \pm 0.7)\,\%$, indicating consistent trapping and transport of water vapor through each tube, with satisfactory recovery rates. For $\approx 8\,\mathrm{g}$ of *Fucus serratus* the average recovery per tube was $(91.4 \pm 3.4)\,\%$ for the custom organic profile discussed in the following section. The larger spread indicating slight differences between a combination of the combustion rate and oxidation of tritium to HTO in each tube. Overall, the consistent and satisfactory recoveries similar to those achieved by Nayak et al. 2019 indicate that the pyrolyser is operating correctly.

### 4.1.2 Recovery Factor and Matrix Mass

Combustion profiles control the temperature of the pyrolyser. A combustion profile comprises a series of segments as illustrated in Figure 4.11. Segments can either be a ramping segment or equilibrium segment, causing the pyrolyser to steadily increase its temperature to a set point or to remain at a specified temperature over a period of time, respectively. A suitable combustion profile steadily fully combusts the sample, allowing for the liberation of tritium, oxidation of tritium to HTO, and subsequent trapping.

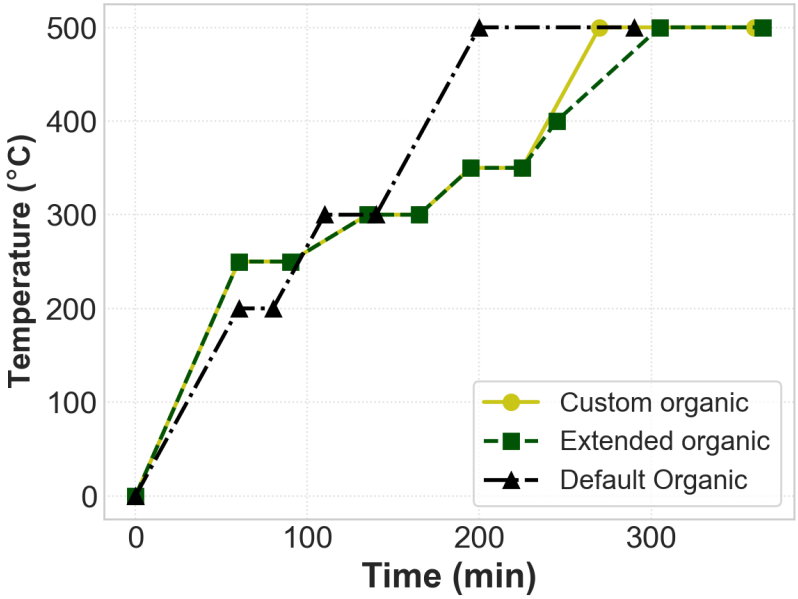


Figure 4.11: Custom organic combustion profiles created along with the default Raddec provided organic combustion profile, and an extended organic profile.

A custom combustion profile was created to handle the complete combustion of the largest possible sample masses, while keeping sufficiently high combustion water yields. As the lab did not have access to an elemental analyzer, a complete and clean combustion was determined by the color and pH progression of the output water and furthermore by measuring the percentage of leftover

ash content within the boat. As a result, the reported recoveries rely on hydrogen content values found in the literature and on the assumption that the combustion water is pure. The hydrogen content for the wheat and bulgur was assumed to be the same. The hydrogen content of the dehydrated wheat reference material is assumed to be the same as from the third interlaboratory comparison $n_H = (6.51 \pm 0.10)\,\%$ (k=2) (N. Baglan, Cossonnet, et al. 2018). A conservative uncertainty of 0.3 (k=1) was used for the bulgur to account for small difference in chemical composition to that of the wheat. The two seaweed species (*Fucus vesiculosus and serratus*) were taken to have a similar hydrogen content of $(4.9 \pm 0.5)\,\%$. The large uncertainty accounts for the differing hydrogen content in dry *Fucus vesiculosus* observed by Ross et al. 2008 and Balina, Romagnoli, and Blumberga 2016, which seems to be similar to that of *Fucus serratus* (Ross et al. 2008).

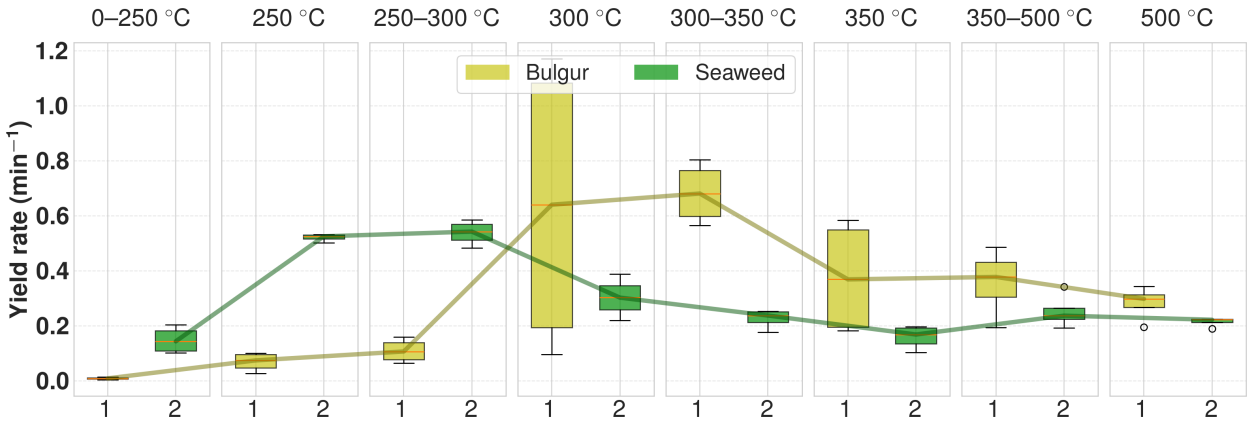


Figure 4.12: A comparison of the yield for *Fucus serratus* and bulgur for the custom combustion profile.

The default organic combustion profile provided by Raddec has been shown to fully combust $4\,\mathrm{g}$ to $8\,\mathrm{g}$ (Nayak et al. 2019, Chen et al. 2022b) for dry vegetation samples. The new custom organic combustion profile was tested on *Fucus serratus* and bulgur samples. The mass of the total combustion water in the bubbler was measured after each segment of the profile. The combustion water yield rates are compared in Figure 4.12. A clear trend emerges that yield rates of the bulgur skews to higher temperatures than that of the seaweed. While the custom organic profile worked for both samples, using the yield rates per segment may allow for more time efficient, matrix specific profiles to be created. For both samples, this profile resulted in clear combustion water for dry sample masses $8\,\mathrm{g}$ to $18\,\mathrm{g}$. The in-depth recovery, pH and color of the combustion water is discussed below for wheat-like samples and the seaweed.

#### 4.1.2.1 Wheat-like Samples

Dry bulgur at $\approx 9\,\mathrm{g}$, $16\,\mathrm{g}$ and $18\,\mathrm{g}$ were fully combusted with respective recovery percentages of $(80 \pm 4)\,\%$, $(86 \pm 4)\,\%$, $(87 \pm 4)\,\%$. The combustion water retrieved for each sample was clear with a pH of 2. The ash content leftover was $1.2\,\%$, $2.4\,\%$, $2.4\,\%$, respectively. The lower ash content for the lower mass sample may be explained by the geometry of the smaller boat used. Having a completely exposed top, allowed for ash content to be blown out of the boat by the supplied air.

The larger boats have a narrower opening with more clearance between the clearing and the ash making this less likely.
The combustion rate of the bulgur was found to vary for the various segments, as displayed in Figure 4.12. It is clear that the majority of the bulgur is combusted at a temperature above $300\,^{\circ}\mathrm{C}$. The combustion rate varies greatly between the 4 samples over the different segments, most notably during the 30 minute $300\,^{\circ}\mathrm{C}$ stable segment, with the only noticeable trend the combustion rate seemed to differ for the quartz tubes on the top row to that of the bottom row. The pH remained stable at 2 to 3 besides the 16g sample, where during the $350\,^{\circ}\mathrm{C}$ to $500\,^{\circ}\mathrm{C}$ ramping segment, the pH jumped to 5 with the color of the combustion water becoming straw yellow. After the following segment the water became clear again and returned to a pH of 2. Overall the recovery rates are similar to or just lower than those achieved by, Nayak et al. 2019 and Chen et al. 2022a, for terrestrial vegetation samples.
The wheat reference material that consisted of whole grains achieved more consistent and higher recoveries to that of the bulgur. Recoveries of $(88 \pm 1)\,\%$ to $(94 \pm 1)\,\%$ for dry sample masses $9\,\mathrm{g}$ to $18\,\mathrm{g}$. Such recovery rates are in line with those achieved by Nayak et al. 2019 who used the default organic profile for a similar wheat reference material, while allowing for 2 to $4.5$ times the dry mass to be combusted. The pH of the combustion water for each repetition (n=4) was consistent at 2 and the water for each was clear.
With the high recovery of the combustion water and consistent pH, it seems that this custom organic combustion profile is suitable for wheat like matrices such as wheat grains and the aforementioned bulgur.

#### 4.1.2.2 Seaweed

The same custom organic combustion profile also resulted in clear combustion water for *Fucus serratus*. The combustion of 10 samples with $8.5\,\mathrm{g}$ to $19.2\,\mathrm{g}$ resulted in recoveries of $(85 \pm 8)\,\%$ to $(103 \pm 11)\,\%$, with an average recovery of $(94.18 \pm 6.00)\,\%$. The large uncertainty originates from the uncertainty in the hydrogen content, therefore the spread of data is not accounted for by the uncertainties. Since the matrix is the same for each, one would expect a tighter clustering of the recovery. Furthermore, the large recoveries around $100\,\%$ indicate that either the local seaweed has larger hydrogen content than that assumed or the combustion water contains significant contaminants. A trend was noticed that 9 of the 10 samples combusted using the aforementioned routine caused the pH to change from 2 to 7 after segment 6 ($350\,^{\circ}\mathrm{C}$ to $350\,^{\circ}\mathrm{C}$). The remaining one stayed consistent at a pH of 2.
A test run with an extended ramping period of $350\,^{\circ}\mathrm{C}$ to $500\,^{\circ}\mathrm{C}$, labelled 'extended organic' in Figure 4.11, was tested for a differing pH behavior. The profile decreased the ramping speed after segment 6 ($350\,^{\circ}\mathrm{C}$ to $350\,^{\circ}\mathrm{C}$). The same *Fucus serratus* sample was combusted with this test profile. 5 samples of mass $8.2\,\mathrm{g}$ to $20.1\,\mathrm{g}$ yielded recoveries of $(89 \pm 9)\,\%$ to $(101 \pm 10)\,\%$ (average $(94.21 \pm 5.94)\,\%$). Each resulting in clear water. 4 of the samples remained consistent at a pH of 2 throughout combustion while 1 moved to a pH of 7 after segment 6, indicating a correlation between the ramping profile and this behavior, however due to the small sample size for both cases no definitive source can be attributed to the behavior of the pH.
The average ash content of the 15 combusted samples was consistent across both combustion profiles at $(17.51 \pm 0.50)\,\%$. Combined with the clear combustion water and high recovery rates, it appears that the custom profile is suitable for combusting seaweed samples up to a mass of $20.1\,\mathrm{g}$,

which is 2.5 times more than what was achieved by Chen et al. 2022a for a variety of terrestrial samples using the default organic profile.

### 4.1.3 Post Combustion Procedure

The recovered combustion water can contain impurities that cause significant quenching in the LSC measurement. The low pH of the wheat samples and some seaweed samples are evidence of this. This section investigates a post combustion procedure to remove the impurities within the combustion water.

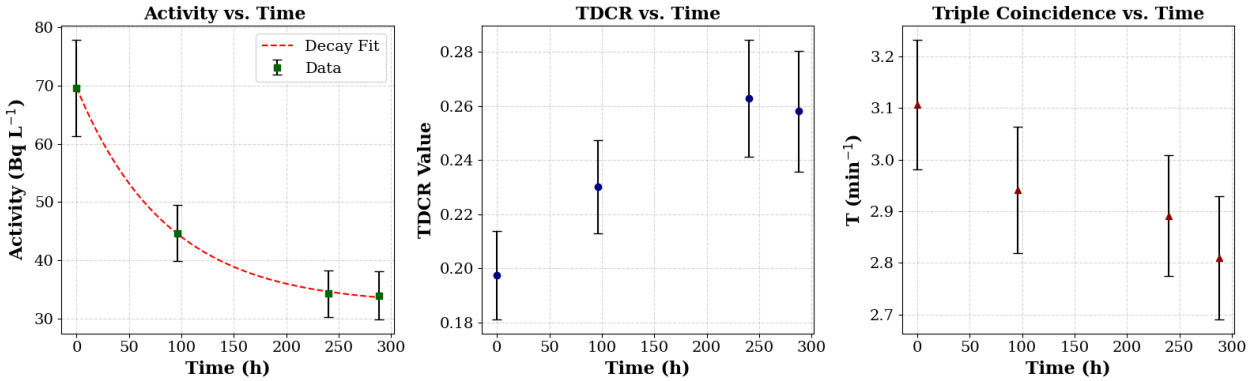


Figure 4.13: The evolution of the activity concentration, TDCR value and, the triple coincidence CPM for the wheat standard for remeasurements.

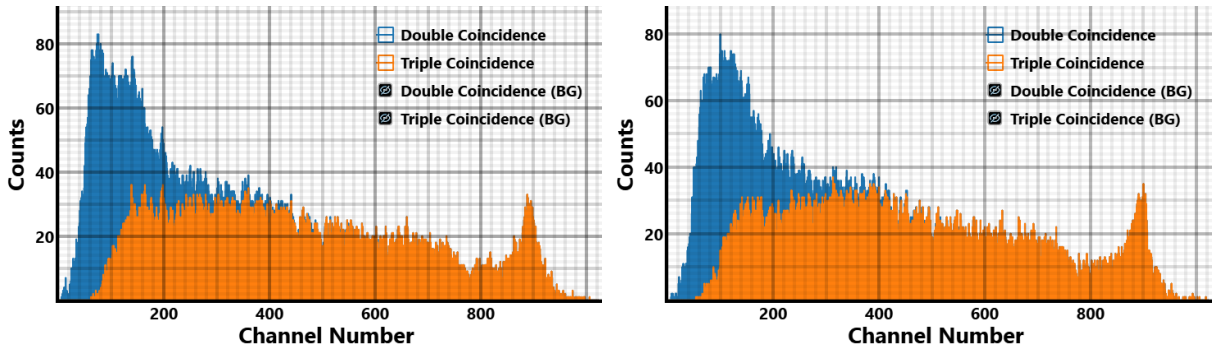


Figure 4.14: A comparison of the double and triple coincidence spectra for the initial spectra (Left) and the remeasured spectra after 300 hours (Right) for the wheat reference material.

Following combustion, samples were mixed with activated charcoal in a 20:1 ratio and filtered to remove organics. This often neutralized samples that were at a pH of 2 to a pH of 4 to 7.

Distillation was found to be an important subsequent treatment. Combustion water from filtered bulgur and seaweed samples were split into two parts: one distilled and the other not. 10 mL of the samples were mixed in a 1:1 ratio with Ultima Gold LLT and measured in the LSC instrument. The bulgur and seaweed triple coincidence counts increased by $(13 \pm 9)\,\%$ and $(10 \pm 7)\,\%$ following distillation, whe the combustion water was distilled. Notably, in both cases, the non-distilled sample had triple coincidence counts below that of the background. The TDCR values of the distilled water

were low $(0.16 \pm 0.17)\,\%$, and $(0.20 \pm 0.09)\,\%$, respectively with large uncertainties compared to typical low quench HTO samples. This likely arises from one of or a mixture of low tritium content in the sample or a high quench. In the latter case, further sample preparation prior to LSC is required.

The activity, TDCR value, and, triple coincidence CPM progressions are illustrated in Figure 4.13, for the wheat reference material. The activity graph indicates the presence of a luminescence impurity compound. The triple coincidence CPM is largely unaffected, however the double coincidence CPM receives significant contributions causing the TDCR value to be underestimated in affected measurements. This is further illustrated in Figure 4.14 where an initial peak at approximately channel number 60 disappears in a follow-up measurement 300 hours later. Since, the extra photons are only detected by double coincidence conditions the origin is likely a photochemical reaction between the scintillator and the combustion water. The time for half of the reaction producing the impurity to disappear is $(60 \pm 4)\,\mathrm{h}$. The efficiency of the final measurement was $(27 \pm 3)\,\%$, which is consistent with normal operating conditions.
A more sophisticated post-combustion treatment using $Na_2O_2$ to neutralize the sample and $KMnO_4$, as performed by Krištof, Chipanovska, and Kožar Logar 2023, may remove the impurity.

## 4.2 Optimization of LSC

The optimization of the LSC methodology was guided by two overarching heuristics.
The first heuristic focused on minimizing the MDA, as lowering the MDA directly improves the sensitivity of low-level tritium detection. Several parameters influencing the MDA were systematically investigated and optimized. These included the selection of the ROI, the measurement time, and the establishment of a well-characterized ("well-known") background spectrum. In addition, the instrumental background was further reduced by optimizing the coincidence detection window, thereby improving the signal-to-background ratio.
The second heuristic aimed to ensure methodological correctness, consistency, and robustness in the data processing procedure. This involved revising the previously implemented activity calculation, introducing a quantification limit, and performing a comprehensive overhaul of the uncertainty estimation framework.
This section presents the individual optimization steps in detail. Optimization were performed on HTO samples and standards. Therefore, the HTO volume was always $10\,\mathrm{mL}$.

### 4.2.1 Quantification Limit

A quantification limit is a chosen cutoff for the result to be satisfactory close to the true value. For low activity environmental samples, uncertainties will be of the order of the activity. Therefore, a quantification limit provides confidence in the accuracy of ones results.

Optimization were primarily implemented by testing the response of the tritium beta spectra for varying input parameters. The activity of the HTO standards utilized was $3\,\mathrm{Bq\,L^{-1}}$ to $180\,000\,\mathrm{Bq\,L^{-1}}$.
To ensure a sufficiently strong signal was used for optimizations a quantification limit was introduced. The quantification limit required the net sample double coincidence CPMs to have a relative uncertainty below $10\,\%$, in accordance with Currie 1968.

It is the standard in the field to work with MDA rather than the LOD. As such the quantification limit was translated into the activity quantification limit (AQL). Which is determined by Equation 4.18

$$\text{AQL} = \frac{10 \cdot \sigma_{D-D_{bg}}}{60 \cdot \epsilon \cdot t \cdot V} \tag{4.18}$$

Where $\sigma_{D-D_{bg}}$ is the uncertainty (k=1) of the net double coincidence CPM, $\epsilon$ is the detection efficiency, t is the total measurement time in minutes, and $V$ is the volume of the sample.
By solving Equation 4.19, the minimum theoretical AQL under normal working conditions may be determined.

$$\frac{\sqrt{D + \sigma^2_{D_{bg}}}}{D - D_{bg}} \cdot \frac{1}{\sqrt{t}} = 0.1 \tag{4.19}$$

Where $D$ and $D_{bg}$ are the double coincidence CPM of the sample and blank, respectively. t is the total measurement time in minutes. The average $D_{bg} \approx 5.06\ \text{min}^{-1}$ and the measurement length was set to 14 hours. Numerically solving for the cutoff of $10\,\%$ relative uncertainty gives a quantification limit of $D \approx 6.13\ \text{min}^{-1}$. Average clean samples have a detection efficiency of $30\,\%$. The AQL for a typical paired observation and well-known background sample is $6.4\,\text{Bq}\,\text{L}^{-1}$, and $4.9\,\text{Bq}\,\text{L}^{-1}$, respectively.

Activities between the MDA and the AQL are classified as detected but not deemed suitable for quantitative analysis.

### 4.2.2 ROI Optimization

ROI optimization aims to identify a channel interval that maximizes measurement efficiency while minimizing background contribution. A commonly used metric for evaluating the suitability of an ROI is the Figure Of Merit (FOM) (L'Annunziata and Kessler 2012, Arun, Vijayalakshmi, et al. 2019):

$$\text{FOM} = \frac{\epsilon^2}{D_{\text{bg}}} \tag{4.20}$$

Where, $\epsilon$ denotes the detection efficiency and $D_{\text{bg}}$ represents the double coincidence CPM of the blank.

ROI optimization was performed by evaluating the FOM across all combinations of minimum and maximum channel numbers defining the ROI. The resulting contour map is shown in Figure 4.15. A similar optimization strategy has been applied to another model of the LSC (Tri-Carb) system, as described in Arun, Vijayalakshmi, et al. 2019. However, the use of the TDCR as a QIP introduces challenges not present when using external QIPs, such as those employed in the Tri-Carb. The TDCR depends solely on the measured activity of the sample. For low-activity samples, the beta spectra exhibit increased relative statistical fluctuations, which can strongly influence the calculated FOM. In such cases, the FOM becomes unstable as an optimization criterion, particularly for determining the lower channel bound.

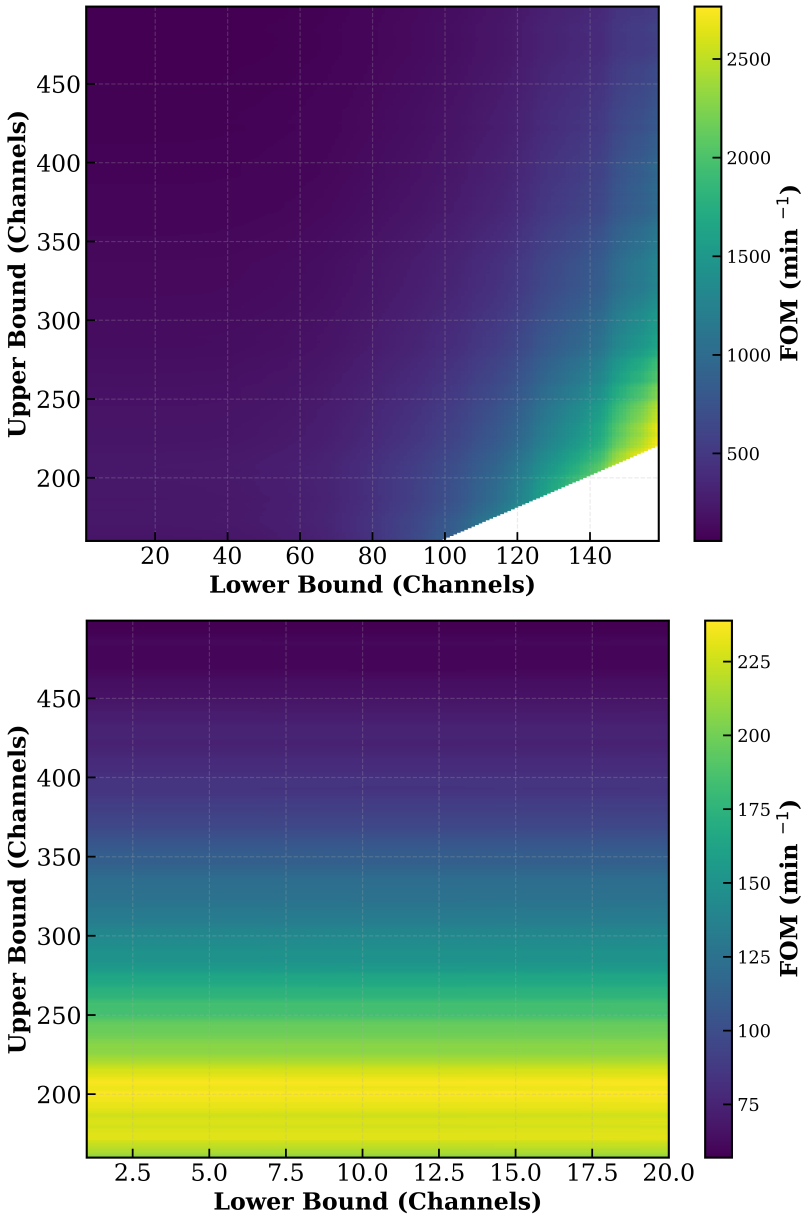


Figure 4.15: Contour plots for $25\,\mathrm{Bq\,L^{-1}}$ HTO standard using the previous TDCR value (Top) and corrected TDCR value (Bottom). The optimized FOM's are found at a ROI of $159$ to $220$, and $20$ to $200$ channel numbers, respectively.

It was observed that samples with activities below $4\,\mathrm{Bq\,L^{-1}}$ yielded FOM maximized for ROIs extending to channel numbers approaching $500$. This behavior is not physically meaningful but instead arises from noise-dominated fluctuations in low-count spectra. To avoid this artifact, ROI optimization was restricted to samples with activities exceeding the AQL, thereby ensuring a consistent and sufficient signal-to-noise ratio.

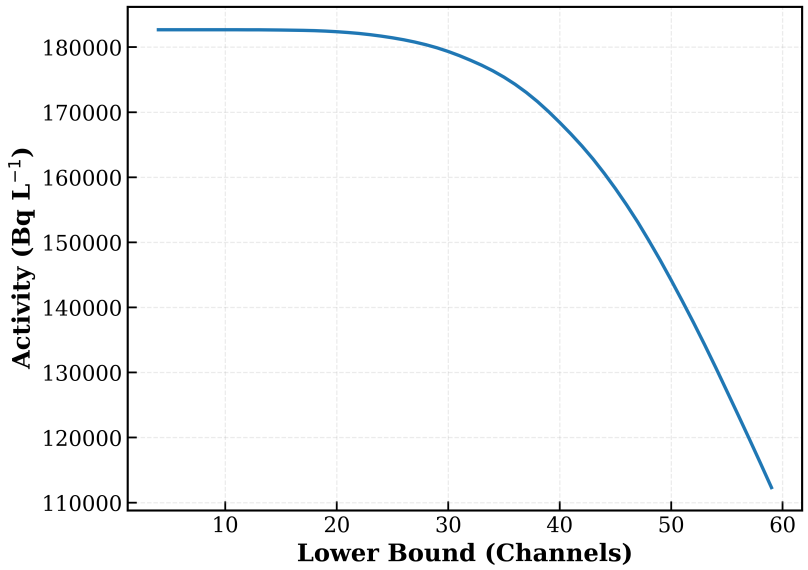


Figure 4.16: Activity for varying minima channel numbers for a $180\,000\,\mathrm{Bq\,L^{-1}}$ HTO standard quenched with $110\,\mu\mathrm{L}$ of nitromethane.

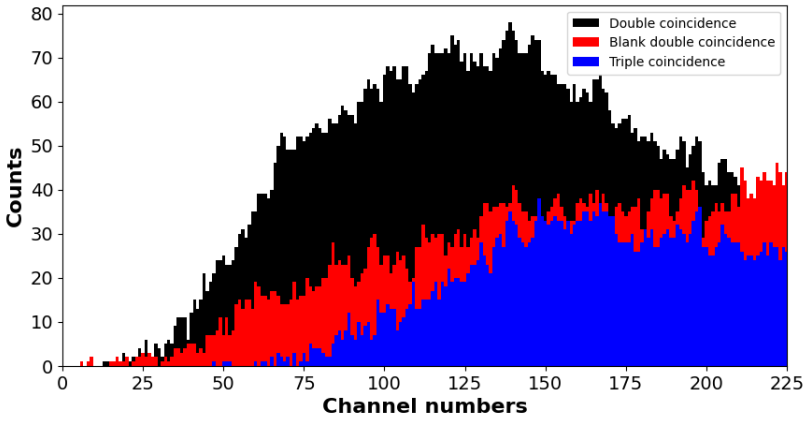


Figure 4.17: The beta spectra for the double and triple coincidences for the sample and blank, respectively.

Furthermore, the TDCR renders the FOM unsuitable for an unconstrained lower-bound optimization. The triple coincidence spectrum typically peaks at higher channel numbers than the double coincidence spectrum. Quenching preferentially suppresses lower-energy photon detection, disproportionately affecting triple coincidences and effectively shifting their apparent spectral maximum toward higher channels relative to that seen for a double coincidence spectrum.

Without imposing constraints, the FOM optimization favors regions that maximize the TDCR, artificially shifting the lower bound to higher channel numbers where the triple coincidence spectrum dominates. This effect is evident in Figure 4.15, where an unconstrained optimization suggests an ROI of approximately channel numbers 150 to 220. Such a selection leads to overestimation of the detection efficiency and a corresponding underestimation of the activity.

This effect is illustrated in Figure 4.16 for a $180\,000\,\mathrm{Bq\,L^{-1}}$ HTO standard heavily quenched with $110\,\mu\mathrm{L}$ of nitromethane. The figure reveals an initial plateau region of channel numbers $0$ to $20$, indicating stable and a physically meaningful efficiency correction. The examples quench level exceeds that expected for environmental samples; therefore, $20$ channels was selected as a conservative upper limit for lower-bound optimization. Under this constraint, the contour plot was recalculated, as shown in Figure 4.15.

ROI optimization was performed using 27 standards spanning activities from $6\,\mathrm{Bq\,L^{-1}}$ to $180\,000\,\mathrm{Bq\,L^{-1}}$ under varying quench conditions. The optimized ROI exhibited a median of $18$ to $192$ channels and a mean of $20$ to $195$ channels, with a standard deviation of $1$ and $15$ channels for the lower and upper bounds, respectively.

The ROI spanning channels $20$ to $195$ was selected as the final optimized region, differing largely from the three manufacturer provided ROI's, tritium ($5$ to $350$), tritium high water load ($5$ to $300$), and tritium low water load ($5$ to $140$). For samples ranging in activity of $12.5\,\mathrm{Bq\,L^{-1}}$ to $50\,\mathrm{Bq\,L^{-1}}$ the MDA of the optimized ROI was compared to the defaults. In the aforementioned order the new ROI lowered the MDA by $(17.1 \pm 4.9)\,\%$, $(26.6 \pm 4.9)\,\%$ and, $(17.1 \pm 6.5)\,\%$, respectively achieving MDA values that would have required multiple extra hours of measurement using these unoptimized ROI's. The previous ROI ($5$ to $220$) used by the lab was decided based on visual examination of the coincidence spectra such as Figure 4.17. The optimized ROI resulted in an average lowering of the MDA for the majority of the samples with an average decrease of $(5 \pm 9)\,\%$ (N=27), with a range of an increase of $4.8\,\%$ to a decrease of $28.4\,\%$, and for $81\,\%$ of samples resulting in a lowering of the MDA. In general the improvement to the MDA ranged from modest to large for the optimized ROI. Beyond the numerical gains, this approach replaces arbitrary visual selection with a systematic methodology, ensuring that ROI determination is grounded in reproducible empirical data. The optimized ROI is similar to the optimized ROI $26$ to $200$ achieved by Arun, Viswanathan, et al. 2021 on a Hidex 300 SL. The upper bound is within uncertainty of this papers optimized value. The conservative lower bound limit chosen in this paper accounts for the difference in optimized lower bound.
Further work into optimization could be increasing the sample size and tightening the activity window to levels more expected of environmental samples. However, such improvements are likely to have small gains.

### 4.2.3 Correction to Calculation Procedure

The calculation procedure previously used to process spectral data and determine activity and MDA was identified to produce incorrect results for low-activity samples. The issue was traced to the implementation of the TDCR calculation. As described in Equation 2.6, the TDCR is defined as the ratio of total triple to double coincidence counts within the ROI. However, the previous laboratory procedure omitted the removal of background contributions.

For low-activity samples, where the background constitutes a substantial fraction of the total counts, this approach leads to an overestimation of the detection efficiency and consequently incorrect uncertainty values. Furthermore, the use of a background-influenced TDCR distorts ROI optimization results.
This causes the previously optimized upper bound for the $25\,\mathrm{Bq\,L^{-1}}$ HTO standard to shift from channel $200$ to $499$. Examination of the sample and blank double coincidence spectra in Figure

4.17, reveals that after an upper limit of approximately 220 channels the blank and sample double coincidence spectra are indistinguishable, meaning larger channel numbers are outside the tritium beta decay region.
For low-activity samples, the background contribution ranges from significant to dominant. For $6\,\mathrm{Bq\,L^{-1}}$ to $50\,\mathrm{Bq\,L^{-1}}$ HTO standards, the background accounts for $(82 \pm 1)\,\%$ and $(32 \pm 4)\,\%$ of the total counts, respectively. As discussed in Section 4.2.2, the relationship between deposited energy and the probability of double and triple coincidence detection is central to this behavior. At higher channel numbers, the probability of triple coincidence detection approaches that of double coincidence detection. Consequently, the TDCR of the background spectrum approaches a value of 1 as the ROI extends into higher channel numbers. When the background contribution is substantial, this effect artificially increases the calculated TDCR, causing the ROI optimization to shift toward unphysical high channel number regions for tritium samples.

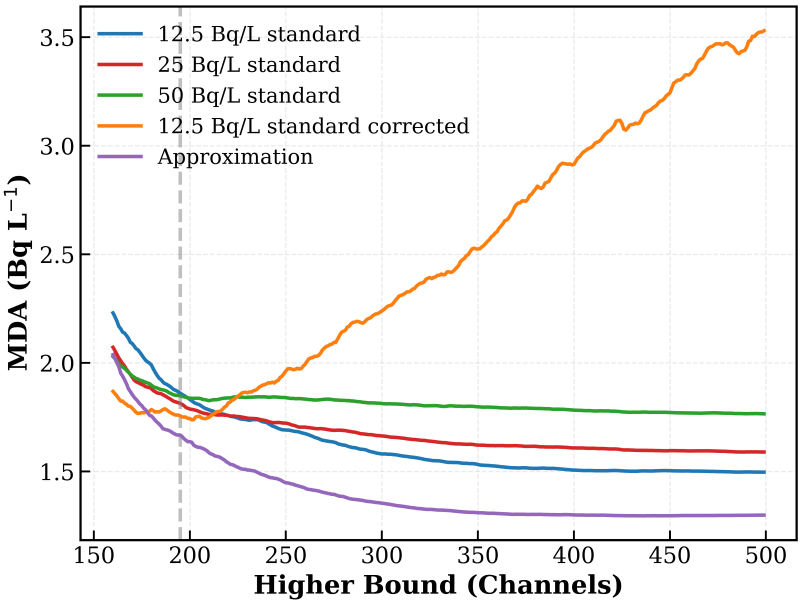


Figure 4.18: Effect of increasing upper bounds on the MDA when using the corrected and previous TDCR calculation. A lower bound 'Approximation' where the TDCR is solely background is provided.

The effect of this incorrect upper-bound optimization is illustrated in Figure 4.18. For standards of $12.5\,\mathrm{Bq\,L^{-1}}$, $25\,\mathrm{Bq\,L^{-1}}$ and $50\,\mathrm{Bq\,L^{-1}}$, the incorrect TDCR implementation produces an apparent reduction in MDA when these unphysical regions are included. A lower-limit case consisting solely of background contributions produces a curve of similar shape, and lower-activity samples approach this limit. For the $12.5\,\mathrm{Bq\,L^{-1}}$ standard, using the ROI obtained from the incorrect method underestimates the MDA by approximately a factor of 2.2.
Uncertainties calculated using the incorrect TDCR implementation differed by approximately $\pm 0.1\,\mathrm{Bq\,L^{-1}}$ compared to those obtained when using the correctly optimized ROI. However, when improperly large ROIs are used, the uncertainty for the incorrect implementation decreases. The opposite behavior is observed for the correct TDCR processing method. Furthermore, the incorrect TDCR implementation fails to reproduce accurate activities for low-activity laboratory standards when us-

ing a largely unoptimized ROI. In contrast, the correct implementation retains accuracy, albeit with larger associated uncertainties.

Following identification of this issue, the TDCR calculation was revised to use background-corrected coincidence counts in accordance with the definition provided by the manufacturer. Notably, this correction was implemented based on physical and statistical considerations prior to confirming consistency with the manufacturer's specification. The previously used procedure therefore appears to have represented a non-standard implementation of the TDCR calculation. High-activity samples are minimally affected by this issue, as background contributions are negligible. In addition, earlier ROI selection relied on visual inspection of the total and background spectra, which constrained the analysis to physically meaningful regions. These factors, combined with the seemingly reasonable activity estimates obtained under such constraints, likely prevented earlier identification of the implementation inconsistency.

### 4.2.4 Uncertainty Optimization

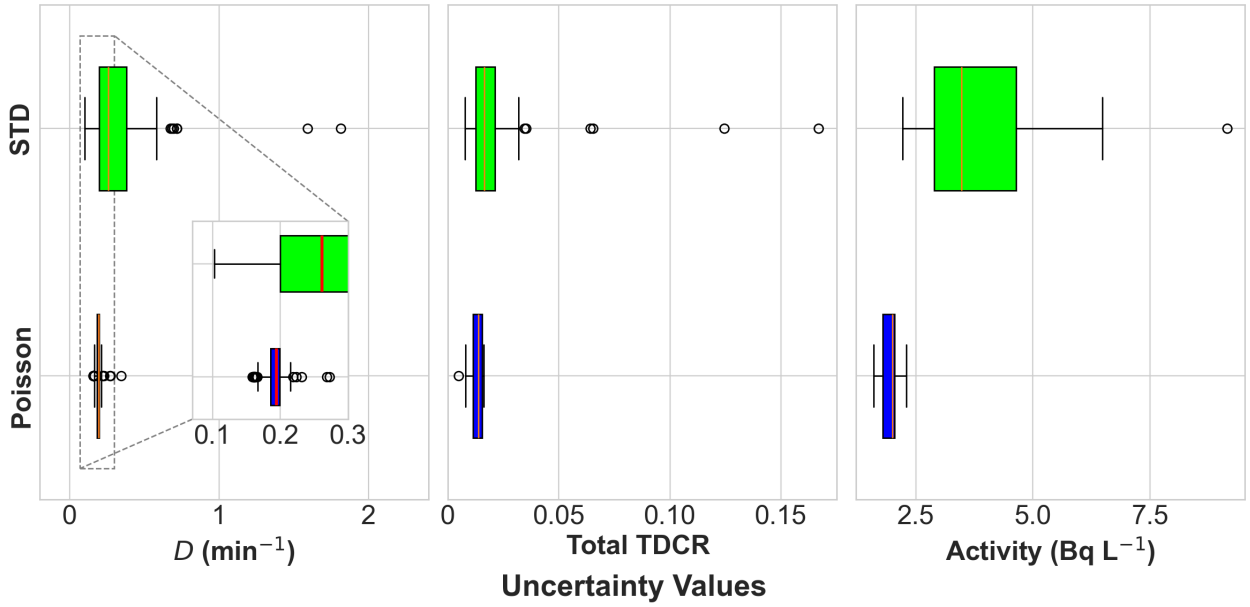


Figure 4.19: Comparison of the uncertainty (k=2) distribution when using standard deviation and Poisson statistics. Double coincidence and TDCR combine the results of 85 low activity samples and the activity uses 16 low-activity samples above the AQL.

Proper uncertainty determination is critical for the accurate interpretation of experimental results, particularly for near-MDA environmental samples, where decision thresholds such as the MDA and the AQL rely directly on uncertainty estimates.
In the previous procedure, several contributions to the overall uncertainty were omitted, including the uncertainty associated with the TDCR and the contributions from linear fitting of the TDCR curve. This omission led to a systematic underestimation of the experimental uncertainty. These values were incorporated into the uncertainty calculation. Furthermore, covariance was omitted in

the calculation, causing an overestimation of uncertainty. Uncertainties before correction acted as a conservative upper bound. The Hidex 300 SL treats triple coincidence detections as double coincidence detections as well. Therefore, the total double coincidence counts depends upon the triple coincidence counts, leading to a non-zero covariance as described in Section 3.3.2. Accounting for covariance led to a drop in activity uncertainty by an average of $(21 \pm 2)\,\%$ for 16 samples ranging in activity of $12.5\,\mathrm{Bq\,L^{-1}}$ to $50\,\mathrm{Bq\,L^{-1}}$.
The current experimental workflow utilizes 14 repeated 1-hour measurements as discussed in Section 4.2.7. A Poisson uncertainty acts as the theoretical counting uncertainty. To determine the Poisson uncertainty the n repetitions are treated as if they were one long measurement of length $n \cdot t$, where $t$ is the length of a single repetition. The Poisson uncertainty solely is influenced by the Poisson decay statistics of the event. This method benefits from universal application to all n. The experimental uncertainty is determined by finding the standard deviation of the average count rate inside the ROI. This method includes uncertainty from drift during measurement, luminescence and electrostatic discharges. The method accuracy of the experimental uncertainty decreases with n.

The difference between the theoretical and experimental uncertainty for the double coincidence CPM, total TDCR, and activity is illustrated in Figure 4.19. The double coincidence CPM and TDCR box plots are composed of data from 85 different samples. These values are independent of knowing the background counts, therefore samples below the AQL were also included. The activity utilized a subset of this data group which was above the AQL. The subset contained 16 samples with activities of $12.5\,\mathrm{Bq\,L^{-1}}$ to $50\,\mathrm{Bq\,L^{-1}}$.
The propagated theoretical uncertainty reduced the estimated uncertainty by a highly variable amount across datasets, with mean reductions of $24.7\,\%$, $17.2\,\%$, and $13\,\%$ for the double coincidence CPM, TDCR, and activity, respectively (Figure 4.19). However, the standard deviations of these reductions were large ($33.4\,\%$, $30.6\,\%$, and $25\,\%$), indicating substantial variability between measurements. The large uncertainties result from several instances where the propagated theoretical uncertainty exceeded the observed experimental standard deviation. This phenomenon is attributed to the limited sample size (n=14); over short measurement intervals, stochastic clustering can result in a deceptively narrow experimental data spread. In these cases, the experimental standard deviation fails as a reliable estimator of the true variance. The theoretical uncertainty therefore serves as a model-based lower bound, preventing the "unphysical" underestimation of uncertainty that can arise from limited statistical sampling

The Hidex 300 SL allows the user to export total double coincidence counts and CPM, but the triple coincidence counts are not directly accessible in the standard output. To compensate, the apparatus returns the TDCR for individual repetitions, as reflected in the recommended TDCR calculation (Equation 4.21). This instrument-specific approach utilizes the TDCR of the total and blank spectra rather than reporting the triple coincidence counts directly.

To simplify covariance calculations and move to a primary counting model (Equation 3.14), the value of $T$ was accessed by exporting the raw spectra through the data processing pipeline. For the custom Hidex template developed in this work, the triple coincidence value is reconstructed by multiplying the reported TDCR by the double coincidence counts. Uncertainty calculations were then performed as if the triple coincidence counts had been initially provided by the hardware.

$$\mathrm{TDCR} = \frac{\mathrm{TDCR}_{Sample} D - \mathrm{TDCR}_{B} D_{bg}}{D - D_{bg}} \tag{4.21}$$

The data cleaning pipeline, discussed in Section 4.3.1, may further lower the total repetitions n. Causing more cases of the previously observed data pooling, to work around this the data processing pipeline reports the theoretical and experimental uncertainty. The final reported value will be the larger of the two values. Furthermore, data cleaning removes cases of uncertainty inflated by outliers. Thus bridging some of the gap between theoretical and experimental uncertainty.

### 4.2.5 Background Management and Progression

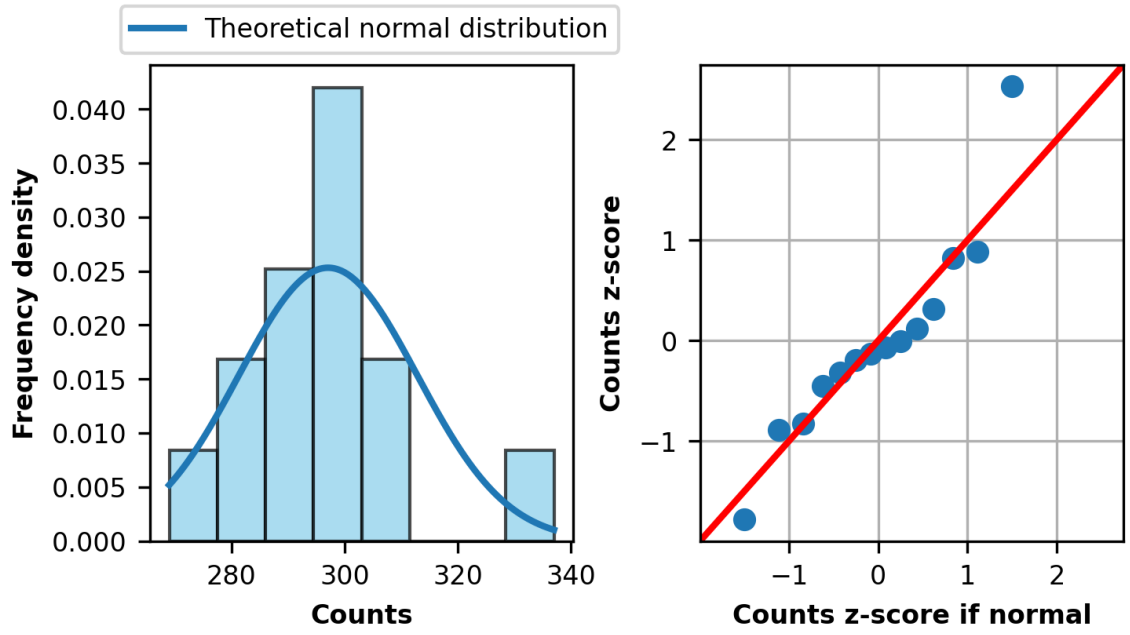


Figure 4.20: (Left) Histogram plot compared to a normal distribution overlay for the frequency of counts. (Right) Q-Q plot of theoretical normal distribution vs actual distribution. Rescaled with z-transform.

For each series of measurement by LSC, a blank sample is measured to serve as paired-observation background in the MDA calculation. This is also required to correct for background contributions for low-activity environmental samples. The blank is switched every month, as the dead water and cocktail begin to separate over longer periods. Tracking of these blank measurements over time is important for quality control. Provided background levels remain stable over time, they may be grouped to create a well-known background.

A well known-background reduces the uncertainty of the calculated activity, lowers the AQL, and the MDA. To assess background stability, a one-way analysis of variance (ANOVA) was applied to groups of average CPMs obtained from the different blanks measured between the months of September and December.
The one-way ANOVA tests the null hypothesis that the means of three or more independent groups are equal. Its application requires that samples are independent, that the groups of data are normally

distributed (or a sufficiently large sample size), and homogeneity of group variances. The different blanks compared ensure independence. All background measurements taken during the month of a specific blank was considered as one group of data. The normality of the data group was tested using the Shapiro-Wilk test, supplemented by visual inspections of histogram plots and quantile-quantile plots (Q-Q plots). All groups yielded a p-value greater than the selected significance level of $\alpha = 0.05$. Therefore, the null hypothesis that the distributions were normal could not be rejected.

In addition, histogram plots and Q–Q plots of the total double and triple coincidence counts accumulated over one hour were examined for each group, an example is illustrated in Figure 4.20. Although the limited number of measurements per group (n=14) restricts definitive conclusions regarding normality, the Shapiro-Wilk test and Q–Q plots were consistent with approximately normal distributions.

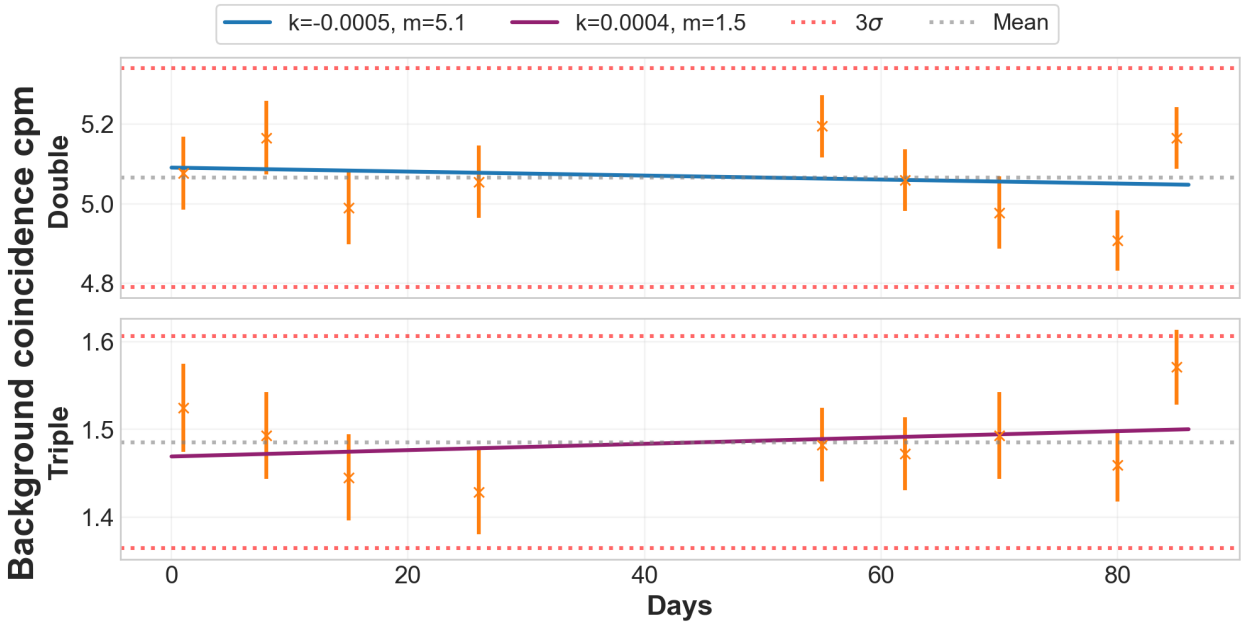


Figure 4.21: Evolution of the double coincidence CPM (top) and triple coincidence CPM (bottom) of the blank samples over time.

Equality of variances between groups was subsequently assessed using Levene's test. Given that the assumptions of independence and approximate normality were satisfied, the test was deemed appropriate. For both double and triple coincidence data, the null hypothesis of equal variances could not be rejected with respective p-values of $0.28$ for double coincidences and $0.38$ for triple coincidences. Given that normality, independence, and homogeneity of variances was satisfied, the assumptions required for the one-way ANOVA were considered met. The ANOVA yielded p-values of $0.11$ for the triple coincidence groups and $0.13$ for the double coincidence groups. In both cases, the null hypothesis could not be rejected. These blanks were considered to have homogenous means.

Stability is visualized using a background control chart to visualize background progression over time. Note blank measurements are now separated by date and not differing blanks. This is displayed in Figure 4.21. A linear fit demonstrated strong background stability over time, with a

fitted slope of $0.0005$ CPM per day. Over an $85$ day period, this corresponds to a $0.3\,\%$ lowering of the average. While the one-way ANOVA demonstrated consistency between blanks, the time-series analysis assessed long-term drift and showed no systematic trend.

Given this consistency, the union of all background measurements was combined to form a single large sample set. Which was used to define the well-known background. Provided the background remains stable, the well-known background can be continually updated with future measurements. However, as shown in Figure 4.22, the reduction in MDA exhibits diminishing returns. Beyond approximately $100$ hours of accumulated background measurement time, the gains are small.

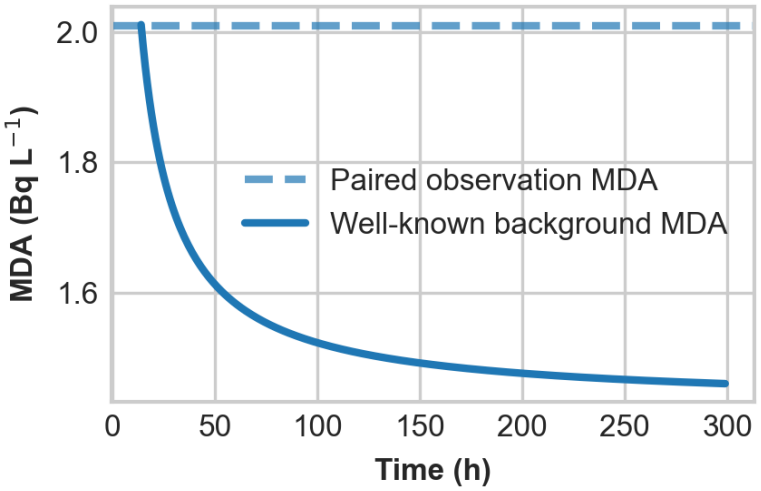


Figure 4.22: Well-known background MDA progression for more consistent blanks contributing to the total background measurement time.

The relative uncertainty of the well-known background was $43\,\%$ lower than that of the corresponding paired blank measurement. This reduction in background uncertainty resulted in an average decrease of approximately $0.2\,\mathrm{Bq\,L^{-1}}$ in the final activity uncertainty.
As discussed in Section 2.3.4, a well-known background has a lower MDA than a paired observation. The condition for which is that the variance of the well-known background $\sigma_B^2 = 0$ (Currie 1968). In practice, provided $\sigma_{S+B}^2 >> \sigma_B^2$, where $\sigma_{S+B}^2$ is the variance of the sample measurement, the well-known background is a justified approximation. A lower-bound case was considered such that there was no average count contribution originating from the radioactivity of the sample $\mu_S = 0$. It was found that for all samples measured the accumulated background will have a variance at least 7 times lower than that of $\sigma_{S+B}^2$. Under these conditions, the assumption of a well-known background was considered justified. However, stricter conditions could be argued for. The use of a well-known background lowered the MDA from $\approx 2\,\mathrm{Bq\,L^{-1}}$ to $\approx 1.6\,\mathrm{Bq\,L^{-1}}$ for a detection efficiency of $30\,\%$ and a sample measurement time of $14$ hours.

Table 4.1: Summary of well-known background statistics applied to 71 HTO samples including standard solutions and environmental samples.

| **Metric** | **Value** |
|---|---|
| Total samples affected | 71 |
| Reduction in MDA (All samples) | $(14.6 \pm 47.5)\,\%$ |
| Samples above MDA (With well-known) | 51 |
| $\hookrightarrow$ Attributable solely to the use of the well-known background | $37.5\,\%$ |
| Reduction in MDA (Samples above MDA) | $(13.5 \pm 27.4)\,\%$ |
| Samples above quantification limit (AQL) | 5 |
| Reduction in MDA (Samples above AQL) | $(24.7 \pm 1.4)\,\%$ |

$75\,\%$ of the 12 blank measurements performed over a six-month period were determined suitable by Equation 3.13 to use a well-known background instead. In total 71 samples were re-evaluated and the reduction in MDA is tabulated in Table 4.1. The large uncertainties in the reduction of the MDA come from the low activity of the samples. Since the overall counts and the background counts are close in value, a small fluctuation caused by moving to a well-known background may cause large shifts in the TDCR. In some cases the MDA was in fact larger after applying the well-known background. However, even in such cases the MDA is relatively lower, since the MDA and activity scale equally by the fluctuations. 5 samples were above the AQL and as such are robust against these fluctuations. Notably the $(24.7 \pm 1.4)\,\%$ reduction in MDA is in line with the theoretical improvements discussed above.

Combining paired observation measurements over time worked for this stable period. Accumulation of measurements taken past this period resulted in a decrease of the Anova p-value to $0.06$, a weak rejection of the null hypothesis. The effect is likely caused by the size of the collective dataset not being large enough or some change in background conditions. The latter may be fixed by performing large background measurements ($\geq$ 50Hr) every time the background is changed. Such measurement lengths are long enough to be individually used as a well-known background and will also provide more accurate data for background progression tracking.
The MDA can be further lowered by improving detection efficiency or by reducing the background CPM, allowing the same MDA to be achieved in shorter measurement times. For example, if the current background decreased from an average of $5$ CPM to $2.5$ CPM, the measurement time required to achieve an MDA of $1.6\,\mathrm{Bq\,L^{-1}}$ for a well-known background would decrease from $14$ to $7$ hours.

For a ROI of $5$ to $350$ channel numbers Hidex advertises background counts of $12$ CPM for the Hidex 300 SL (Hidex Oy 2023). For the same ROI we achieve $11.7$ CPM. Newer models of liquid scintillation counters, such as the Hidex 300 SL Super Low Level and the Hidex Ulla, advertise background CPMs of $3$ and $1$, respectively. The Quantulus 1220 has been reported to achieve background CPMs between $0.5$ and $0.8$, with detection efficiencies ranging from $21\,\%$ to $26\,\%$ (Baburajan et al. 2020, Schäfer, Hebert, and Zeiske 2000, Varlam et al. 2009).
Background levels can also be reduced by additional shielding. Schäfer, Hebert, and Zeiske 2000 demonstrated that moving a Quantulus 1220 $47\,\mathrm{m}$ below ground halved the background CPM. Similarly, encasing the counter in lead shielding may also reduce the effects of cosmic rays.

### 4.2.6 Coincidence Window Optimization

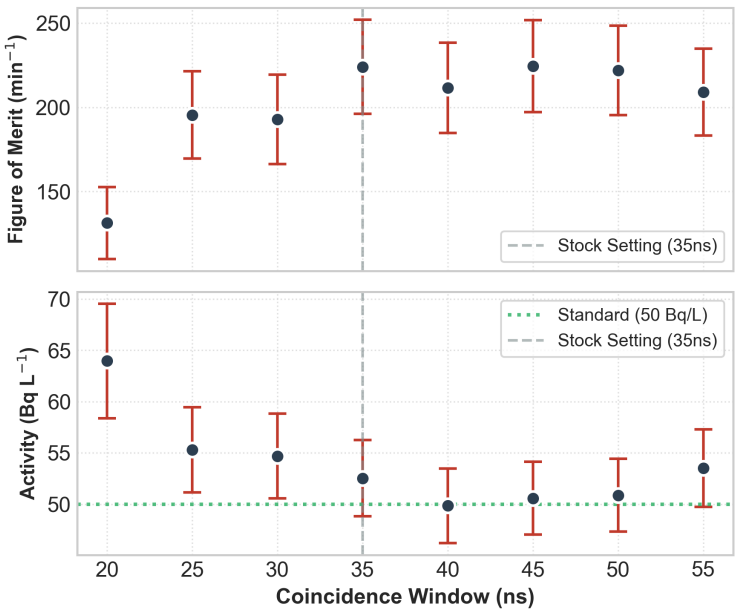


Figure 4.23: Evolution of the FOM, and activity for increased coincidence window lengths (k=2).

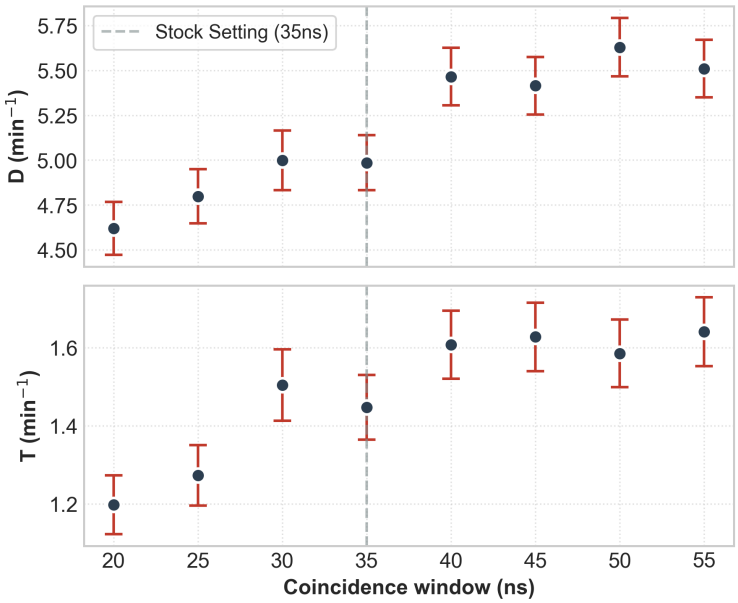


Figure 4.24: Evolution of the background double and triple coincidence CPM for different coincidence window lengths (k=2).

The coincidence window is a time buffer following the initial photon detection in the LSC instrument that groups any further photons detected within that period as a single measurement. An optimized coincidence window balances being long enough to catch all photons released from a

decay event while being sufficiently short to limit background contributions. By optimizing the coincidence window, one can further reduce the MDA.

The Hidex 300 SL's stock coincidence window is $35\,\mathrm{ns}$. Coincidence windows in $5\,\mathrm{ns}$ increments were tested for $20\,\mathrm{ns}$ to $55\,\mathrm{ns}$ on a $50\,\mathrm{Bq\,L^{-1}}$ HTO standard. The measurements consisted of $14$ one-hour repetitions, and the CPM of the blank was used in all activity determinations. The relationship between the coincidence window, the FOM, and activity ($k = 2$) is displayed in Figure 4.23, with the FOM used as an optimization parameter as described in Section 4.2.2.

With the exception of the $20\,\mathrm{ns}$ window, all other coincidence windows are within two standard deviations of one another. A noticeable plateau region occurs after $35\,\mathrm{ns}$; for the activity, all measurements at or after $35\,\mathrm{ns}$ are within the uncertainty of the lab-created standard's activity.

Being conservative, this indicates that coincidence windows of $35\,\mathrm{ns}$ to $55\,\mathrm{ns}$ are indistinguishable for $50\,\mathrm{Bq\,L^{-1}}$ samples. The lower values of this range are likely better for lower activity samples, as background will represent a relatively larger proportion of the overall counts compared to the $33\,\%$ observed in the $50\,\mathrm{Bq\,L^{-1}}$ HTO sample. As illustrated in Figure 4.24, there is a noticeable jump followed by a plateau in both triple and double background coincidence counts ($k = 2$) after $35\,\mathrm{ns}$. The final optimized routine thus retained the manufacturer's preset value of $35\,\mathrm{ns}$, a setting also determined to be optimal by Song et al. 2016.

### 4.2.7 Measurement Time Optimization

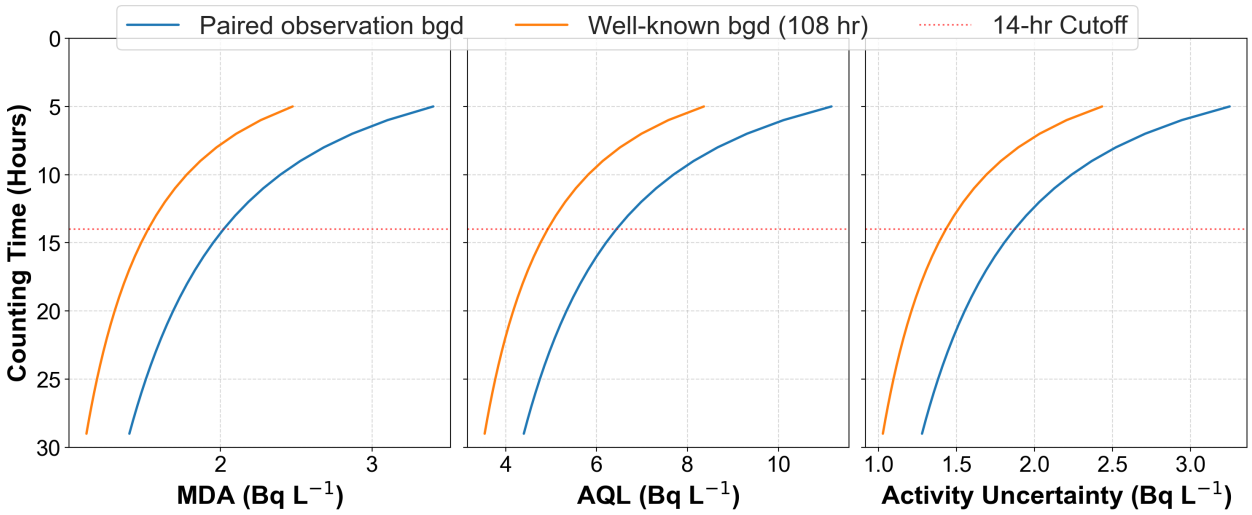


Figure 4.25: Evolution of MDA, AQL, and activity uncertainty with time.

Increasing the total measurement integration time, and consequently the number of counting repetitions, directly reduces the measurement uncertainty, the MDA, and the AQL. Furthermore, an expanded sample size facilitates more rigorous data-cleaning processes, rendering the final activity calculation more robust against stochastic outliers. The measurement time for this study was optimized to balance analytical sensitivity with operational throughput, seeking the point of maximum practical return.

The fundamental Poisson statistics governing radioactive decay dictate the non-linear improvements in uncertainty and detection limits relative to time. This relationship is illustrated for both

paired observations and well-known background scenarios in Figure 4.25. For these calculations, the background was assumed to correspond to the observed CPM of the well-known background ($D_{bg} = 5.056$ CPM) with a detection efficiency of $30\,\%$. As expected, all three metrics MDA, AQL, and activity uncertainty evolve according to a $1/\sqrt{t}$ relationship.

Given that these metrics exhibit identical functional forms, optimization was performed specifically on the MDA. Figure 4.26 displays the evolution of the MDA gradient ($\Delta \mathrm{Bq\,L^{-1}}/\Delta t$) alongside the hourly percentage improvement. The data suggests that the system enters a "stability phase" characterized by diminishing marginal returns after approximately 11 hours of integration.

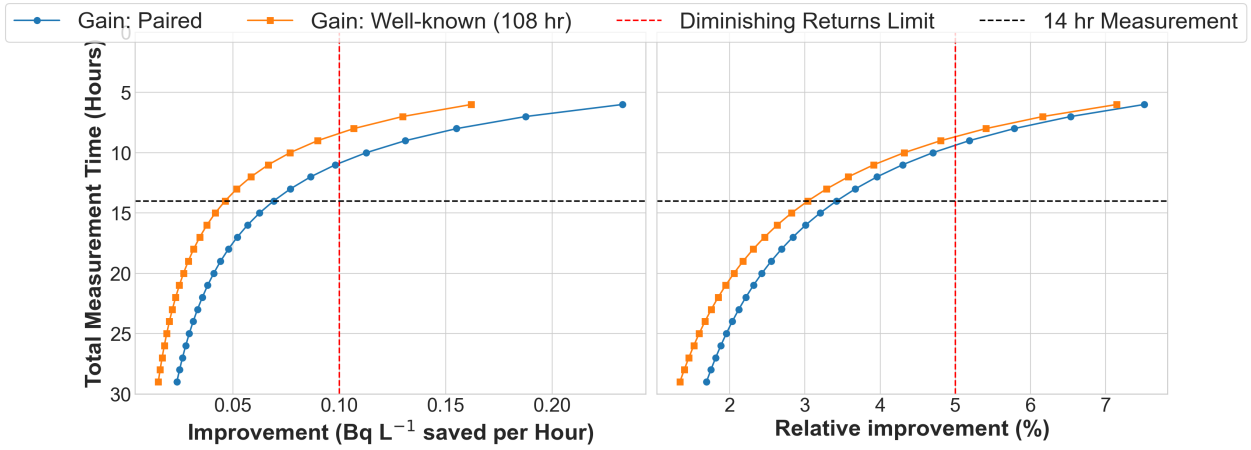


Figure 4.26: Diminishing returns of increased measurement time for lowering the MDA. **Left:** Improvement of $\mathrm{Bq\,L^{-1}}$ saved for each new hour of measurement. **Right:** Relative lowering of MDA for an extra hour of measurements.

An optimized duration of 14 hours was selected based on three reasons:

1. **Analytical Benchmarking:** 14 hours represent the minimum integration time required to achieve a paired observation MDA of $2\,\mathrm{Bq\,L^{-1}}$. This provides a clear, integer benchmark for assessing instrumental performance and simplifies quality control.

2. **Statistical Efficiency:** At 14 hours, the system has operated for several hours within the stability zone. The marginal improvement rate at this point ($\approx 3.5\,\%$ per hour) ensures that the primary statistical gains of the Poisson distribution have been realized.

3. **Algorithmic Robustness:** The 14-hour window provides a sufficiently large population size for the non-parametric outlier rejection protocols (z-score and interquartile range filtering) discussed in Section 4.3.1. A larger sample set ensures that the statistical boundaries used for data cleaning are stable and representative of the true background distribution.

## 4.3 Data Analysis Optimizations

This section discusses additions made to the analysis of the Hidex 300 SLs measurement data, including a custom data cleaning protocol, and the development of a bespoke PySide 6 application to extend the functionality of the Hidex 300 SL.

### 4.3.1 Data Cleaning

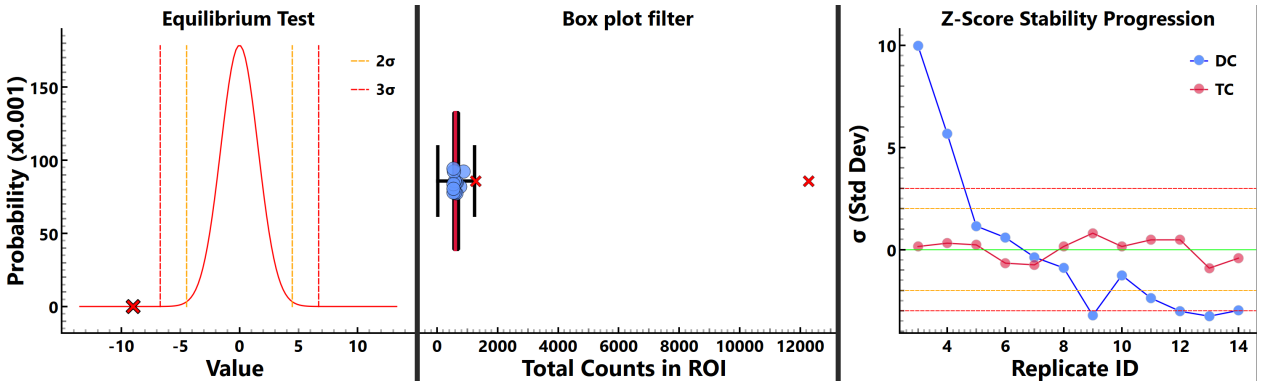


Figure 4.27: Visualization of the three data-cleaning processes. **Left:** Distribution of the adapted signs test. **Middle:** Box plot of total counts per repetition with $k = 3.5$. **Right:** Z-score progression of total counts over repetitions for double and triple coincidences.

A three-step data processing procedure was implemented in order to identify and remove outliers. Extreme outliers resulting from large electrostatic spikes are removed using quartile filtering. Z-score tests remove moderate outliers and signs test reject unstable datasets.

Over multiple measurement cycles, large outliers were repeatedly identified in the first measurement repetition, indicating that electrostatics discharges were responsible for the spike in counts. Statics can either be induced during sample preparation or as the sample is moved to the measurement chamber. While an ionizing gun is used to neutralize these charges, residual statics occasionally persisted. Quartile filtering was performed by partitioning the dataset into four equal parts using the median ($q_2$) and the subsequent medians of the lower and upper ($q_1$ and $q_3$) halves. Unlike the mean, these positional statistics are robust against extreme values, ensuring that a single large electrostatic spike does not skew the center of the dataset and mask its own presence The interquartile range (IQR) was determined by the difference between the first and third quartiles. The range of acceptable values was defined according to Equation 4.22:

$$q_1 - IQR \cdot k \leq x \leq q_3 + IQR \cdot k \tag{4.22}$$

Where $k$ is Tukey's outlier coefficient. $k$ generally takes a value of $1.5$, however instances of tight data grouping, due to the small dataset sizes resulted in small IQR values and the unintended exclusion of non-outlying data points. Therefore, a more lenient value of $3.5$ was chosen. Quartile filtering is illustrated using box-whisker plots as shown in Figure 4.27.

After the removal of extreme outliers, moderate outliers were identified using a simple z-score. A lenient approach was applied, accepting data within three standard deviations of the group mean. The z-score is unique among the three tests in that its primary goal is to identify outliers that may not originate from electro-static discharges. Consequently, it is the only test applied to both double and triple coincidences. This approach effectively removes moderate statistical outliers. The progression of the z-scores is illustrated in Figure 4.27.

Outliers for stable datasets are handled by the above methods. A minority of datasets exhibited non-stable behavior. Such behavior resulted from a very large electrostatic spike. Counts during this measurement hour were approximately 20 times that of any other repetition. Subsequent measurement hours followed a continual trend of counts decreasing. Equilibrium had not been achieved after the large perturbation. A variation of a signs test was implemented to reject such events. For each data point the subsequent hours measurement is subtracted. The sign of the operation was mapped to -1,+1. The sum of this binary group is evaluated to a Monte Carlo (N=200 000) simulation of this procedure for normally distributed data. The distribution over measurement repetitions was shown to be normal in Section 4.2.5, for typical low activity samples. This simulation was carried out individually for groups sizing of 2 to 97 components, with values tabulated in Table B.1. A batch-wise rejection criterion was applied to any dataset where the observed sum exceeded $3\sigma$ of the simulated mean, prompting a complete re-measurement of the sample.

Table 4.2: Summary of data cleaning pipeline performance across 85 samples.

| **Metric** | **Value** |
|---|---|
| Total Samples Evaluated | 85 |
| Samples Rejected (Non-equilibrium) | 3 |
| Total Repetitions (Accepted Samples) | 988 |
| Total Repetitions Rejected | 50 (5.1 %) |
| Affected Samples (requiring filtering) | 45 |
| First-Hour Outlier Frequency | 80 % |
| Mean Activity Reduction (Filtered Samples) | $(34 \pm 27)$ % |
| Samples Preserved (No first-hour bias) | 40 |

The performance of the data cleaning pipeline was tested across 85 samples, as tabulated in Table 4.2. In total 3 samples were completely rejected for not reaching equilibrium conditions. The remaining 82 samples totaled to 988 repetitions, of which 50 were rejected, by either the z-score or the quartile filtering. The 50 rejections corresponded to 45 samples. 80 % of the rejections came in the first repetition, indicating contribution from luminescence or electrostatic discharges. These contributions diminish after the first hour of measurement. Filtered samples saw an average decrease of activity by $(34 \pm 27)$ %. The large standard deviation arising from the combined contributions of interquartile and z-score filtering. The former removing large electrostatic pulses resulting in larger relative drops compared to the latter.

### 4.3.2 Data Processing Application

The Hidex 300 SL operates by requiring the creation of a measurement template prior to data acquisition. The variables and ROI defined in this template are determined prior to measurement and are not typically modified post acquisition within the standard workflow. While this approach ensures consistency, it is highly sensitive to human error and lacks flexibility. In applications such as combustion water analysis, where sample volumes and MCFs factors may vary, a more adaptable data treatment workflow is essential. Furthermore, the template-structured approach can

be inflexible under certain conditions, for example, going from measuring just tritium samples to tritium and $C^{14}$ samples, multiple backgrounds and so on. For such cases a new template with adapted matrix calculation logic is required.

To address these limitations, a data-processing graphical user interface application was developed using PySide 6. The application imports CSV files containing spectral data generated by the default export driver of the Hidex 300 SL. The workflow is divided into four main modes: variable input, data processing and table viewing, data visualization, and data exporting.

#### 4.3.2.1 Variable Input

The initial window allows the user to load the spectral CSV file. Once loaded, a grid representation of the measurement tray is displayed, indicating the physical positions of the samples (Figure C.1). The user may modify the ROI, define a well-known background, adjust the measurement duration, and specify the measurement date for any supported radionuclide using the widget located above the Home button.

The buttons located below the Home button enable interaction with the tray grid. The user may define the sample name, MCF, volume, collection date, and radionuclide type for each position. The background position can be reassigned to any tray position, and multiple background positions may be specified. When multiple backgrounds are defined, the application automatically selects the background closest in measurement date to the corresponding sample. Additionally, the user may manually remove outlier repetitions from the analysis during this stage.

#### 4.3.2.2 Data Processing and Table Viewing

The data processing stage implements the procedure described at the end of Section 4.2.3, in conjunction with the data-cleaning methods outlined above. Once processing is complete, the relevant results are displayed in tabular form (Figure C.2).

The upper table presents the raw results prior to data cleaning, while the lower table displays the filtered results after outlier removal. Interactive controls allow the user to hide selected rows or columns and to filter results by radionuclide. A separate table lists the removed repetitions and identifies the corresponding samples. Additionally, Boolean indicators are included to show whether the well-known background criterion was satisfied and whether the calculated activity exceeds both the AQL and the MDA.

#### 4.3.2.3 Data Visualization

The application includes a spectral viewer accessible via a dedicated button, which provides a preview of the total measured spectrum. Upon selection, the user can display individual repetition spectra, combined double and triple-coincidence spectra, background-subtracted coincidence spectra, and visualizations of the data-cleaning procedure (Figure 4.28). The data-cleaning plots are further discussed in Section 4.3.1.

The repetition level visualization enables the user to inspect and validate the removal of specific repetitions. Removed repetitions are clearly indicated in a separate spectral plot for transparency.

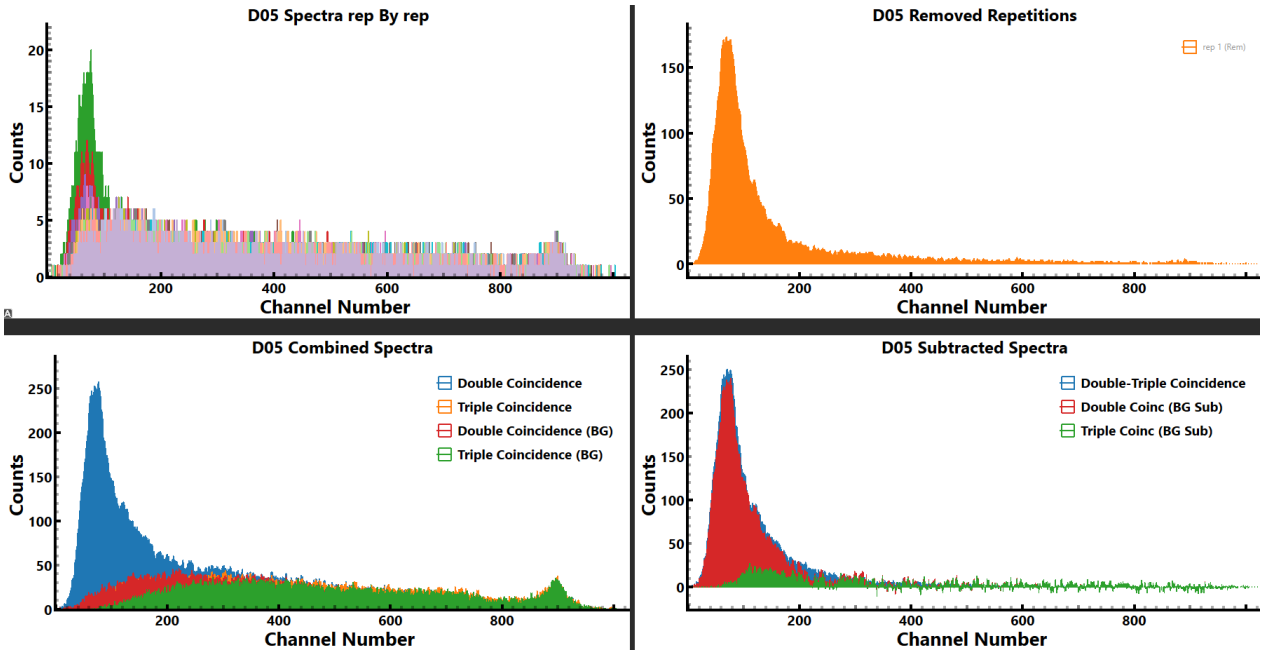


Figure 4.28: Spectra plots created from the exported data. **Top Left:** Single repetition spectra. **Top right:** Outlier spectra. **Bottom left:** Combined double, triple coincidence spectra for sample and background, respectively. **Bottom Right:** Double and triple coincidence background subtracted spectra and triple subtracted from double coincidence subtracted spectra.

#### 4.3.2.4 Data Exporting and Benefits

The application allows for the export of any selected combination of rows or columns from the results tables to CSV or XLSX format. The user may also choose to export results corresponding to a single radionuclide when multiple radionuclides are analyzed simultaneously. Furthermore, the user may select whether to export raw or filtered datasets.

The primary advantage of the developed application compared to the native Hidex software is its post-measurement flexibility. The ROI, well-known background parameters, background positions, and the number of background measurements can be modified after data acquisition. The application also supports systematic outlier removal and integrates data-cleaning procedures directly into the analytical workflow, while preserving user control over whether raw or filtered data are exported.

The application allows the user to save their custom parameters for a specific CSV file in a JSON file, providing a simple way to load past settings.

In the native template-based system, changes to these parameters require modification or recreation of the measurement template prior to acquisition. The developed application removes this dependency by enabling post-measurement adjustment of analysis parameters.

For extended measurement sequences containing multiple samples, it may be advantageous to include multiple blank measurements to ensure temporal proximity between the blank and sample measurements. The application supports this by allowing multiple background positions and automatically selecting the most temporally relevant background during analysis, without requiring template modification.

The visualization of the data-cleaning process further enhances transparency and increases user confidence in the integrity of the analysis.

Overall, the application shifts the analytical workflow from a rigid, template-dependent structure to a flexible post-measurement framework. By separating data analysis from the Mikrowin software, it enables modification of key analytical parameters without requiring remeasurement. This design supports reproducibility, transparency, and adaptability in LSC data analysis.

# Conclusion and Outlook

Accurate measurements of OBT and TFWT are vital for monitoring the environmental effects of tritium discharges from nuclear power plants and for estimating the annual dose to the public. Achieving such accuracy requires highly refined protocols across the entire analytical chain from the initial sample collection and preparation through to the final measurement. In this thesis significant progress has been made in developing a custom laboratory procedure to extract and measure OBT concentrations in wheat and seaweed matrices. This progress centered on extracting OBT via combustion using the newly acquired Raddec gen IV PYROLYSER, alongside optimizing the measurement process using the Hidex 300 SL.

Work on the pyrolyser focused on verifying the performance of the machine, assessing the suitability of a custom cold trap, and creating a custom combustion profile that facilitates the complete combustion of matrix masses of $8\,\mathrm{g}$ to $18\,\mathrm{g}$ of dry material.

An ice-saltwater mixture in a Dewar flask over a 6-hour combustion cycle was shown to be a suitable cold trap, achieving recoveries of $(97.0 \pm 0.5)\,\%$ when combusting a sand and deionized water mixture of $\approx 5\,\mathrm{g}$. This further confirms that the transport of gases throughout the machine is operating correctly. The six independent quartz tubes were demonstrated to give consistent and satisfactory recovery rates. With an average recovery of $(94.4 \pm 0.7)\,\%$ and $(91.4 \pm 3.4)\,\%$ when combusting $\approx 5\,\mathrm{g}$ of de-ionized water mixed with $\approx 7.4\,\mathrm{g}$ acid washed sand and $\approx 8.5\,\mathrm{g}$ of *Fucus serratus*, respectively.

The custom combustion routine differed from the default organic program by maintaining temperatures of $250\,^{\circ}\mathrm{C}$ to $350\,^{\circ}\mathrm{C}$ for extended periods. The default organic procedure has been shown to combust terrestrial vegetation samples with masses of $4\,\mathrm{g}$ to $8\,\mathrm{g}$ (Nayak et al. 2019, Chen et al. 2022a), with recoveries of $87\,\%$ to $94\,\%$. The new custom combustion profile yielded recoveries of $(80 \pm 4)\,\%$ to $(87 \pm 4)\,\%$ for store-bought bulgur with masses of $9\,\mathrm{g}$ to $18\,\mathrm{g}$. Furthermore, a reference wheat material obtained a recovery of $(88 \pm 1)\,\%$ to $(94 \pm 1)\,\%$ for masses of $8\,\mathrm{g}$ to $17\,\mathrm{g}$. This is in line with the $92\,\%$ recovery achieved for a similar reference material by Nayak et al. 2019. The pH progression for the bulgur sample was tracked over the segments and remained mostly consistent at approximately 2, except one sample which jumped to a pH of 5 before returning to 2 in the following segment. Overall, the new combustion routine was determined to facilitate the complete combustion of matrix masses double that of the default organic program, with the trade-off of an extra 70 minutes of run time.

Furthermore, this new combustion profile was shown to produce clean combustion water for *Fucus serratus* samples ranging in mass from $8\,\mathrm{g}$ to $19\,\mathrm{g}$, achieving recoveries of $(85 \pm 8)\,\%$ to $(100 \pm 10)\,\%$. Moreover, the pH progression inconsistently jumped from 2 to 7 for segments above temperatures of $350\,^{\circ}\mathrm{C}$, that correlated with the temperature ramping rate. Further work should

examine the chemical composition of the seaweed along the combustion chain. However, regarding the criterion of creating clear combustion water with high recoveries, the new combustion profile was shown to be highly suitable for the above-mentioned mass range for seaweed.

A simple pre-measurement procedure was established for the combustion water, where it was determined that distillation was required to achieve a triple coincidence CPM greater than that of the background. However, even after filtration using activated charcoal and distillation, significant quench or low activity was found in the seaweed and bulgur samples, resulting in poor TDCR values. In the reference wheat material an impurity thought to originate from chemical luminescence with a half life of $(60 \pm 4)\,\mathrm{h}$ was observed. After the luminescence contributions ended the detection efficiency of the wheat material was in line with normal operating conditions.

Further development of the laboratory procedure regarding the combustion process and water processing should focus on creating a method to determine the hydrogen content in the matrix before and after measurement. This would allow for the verification of complete sample combustion. Furthermore, chemical analysis of the combustion water after processing is vital for the correct determination of the MCF, along with identifying possible quenching compounds. To reduce significant quenching, further neutralization and purification steps should be examined. The use of $Na_2O_2$ for neutralization and $KMnO_4$ for purification during the distillation has been shown to be effective by Krištof, Chipanovska, and Kožar Logar 2023.

Significant corrections and optimizations were made to the previous lab protocol using the Hidex 300 SL. Corrections were made to the TDCR calculation; the previous method omitted the removal of background contributions, which resulted in incorrect activity determinations for poor ROIs and led to errors during ROI optimization. Furthermore, the uncertainty calculation was revised to include contributions from the TDCR and quench curve. The previous omission of these variables led to a significant underestimation of the activity uncertainty. Finally, the covariance between double and triple coincidences was accounted for, leading to a $(21 \pm 2)\,\%$ decrease in the corrected activity uncertainty.

The optimized ROI was found to be channel numbers $20$ to $195$, offering significant improvements ($(17.1 \pm 4.9)\,\%$, $(26.6 \pm 4.9)\,\%$ and, $(17.1 \pm 6.5)\,\%$) over the three manufacturer-designated tritium ROIs ($5$ to $350$, $5$ to $300$ and, $5$ to $140$). Furthermore, reducing the MDA by an average of $(5 \pm 9)\,\%$ for the labs previously used ROI of $5$ to $220$. The optimal coincidence window was determined to be $35\,\mathrm{ns}$ to $55\,\mathrm{ns}$ using the FOM. A window of $35\,\mathrm{ns}$ was selected due having overall smaller background contributions, thereby verifying the manufacturer's default parameter as the optimal value.

The establishment of a well-known background lowered the MDA of affected samples approximately $20\,\%$ under normal operating conditions. Such a reduction would require approximately $8$ hours of additional measurement time per sample. Overall, 71 samples were determined to meet this well-known background criteria, 19 of which rose above the MDA as a direct result. An optimal measurement time of 14 one-hour repetitions was established, achieving an MDA of $2\,\mathrm{Bq\,L^{-1}}$ under normal operating conditions for a paired-observation background measurement. Furthermore, these 14 repetitions provided sufficient statistics for outlier filtering.

A custom data cleaning pipeline was established to remove outlier repetitions. Within a group of 85 samples, $53\,\%$ were affected by outliers occurring mainly during the first hours of measurement. The pipeline rejected $5.1\,\%$ of measurement repetitions, resulting in a mean activity reduction of $(34 \pm 27)\,\%$.

Finally, a custom PySide 6 application was developed to extend the core functionality of the Hidex 300 SL, allowing for post-measurement alterations to the ROI, background location, well-known background values, volume, MCF, sample isotope, and outlier selection. The application incorporates the aforementioned data cleaning pipeline, facilitating the visualization of the filtering process and measurement spectra. Furthermore, the application streamlines the conversion of raw spectra data into a final spreadsheet format, thereby increasing transparency, reducing input errors, and ensuring reproducibility.

The current measurement protocol has been verified to operate correctly for lab-created low activity HTO standards of $12.5\,\mathrm{Bq\,L^{-1}}$ to $50\,\mathrm{Bq\,L^{-1}}$. Verification using certified standards remains as the final validation step for the LSC protocol. The results of the 2026 interlaboratory wheat matrix (PROCORAD 2025) will be reported after the completion of this thesis and will inform subsequent alterations to the method.

Regarding possible further optimizations, the current linear model applied to the quench curve wasn't investigated in this paper. However, the overall decrease in uncertainty with a higher order polynomial model would be minor, as the linear model currently represents a minority contribution to the total uncertainty. The introduction of external shielding would likely lower background and thus the MDA further. Additionally, the dark exposure time could potentially be reduced from 24 hours to 4 hours by utilizing LED lighting, as demonstrated by Ohki et al. 2021. A standardized pre-combustion processing procedure should be developed, focusing on limiting the isotopic exchange of tritium with environmental hydrogen during collection, transportation, processing, and storage. Furthermore, a procedure to remove E-OBT tritium from the sample should be established, similar to methodologies developed by F. Pointurier et al. 2003 and Kuwata et al. 2025.

Finally, the lab could investigate the practicality of creating internal OBT standards by the manipulation of E-OBT levels in a sample. This could theoretically be achieved by isotopic exchange of hydrogen with tritium by immersing the dried sample in HTO of a known activity. Which is the reverse of the previously mentioned process to remove E-OBT from the matrix (Kuwata et al. 2025). The creation of such standards would provide a valuable diagnostic tool to investigate the continual correct operation of the procedure, verification that the procedure works for new matrices not tested in this paper, and to be a reference sample for interlaboratory comparisons with associated laboratories.

# References


Arun, B., I. Vijayalakshmi, et al. (Jan. 2019). "Optimization of Liquid Scintillation Counter for Tritium Estimation in Water Samples". In: *Radiochemistry* 61.1, pp. 61–65. DOI: 10.1134/S1066362219010090.

Arun, B., S. Viswanathan, et al. (Mar. 2021). "Study of Triple to Double Coincidence Method for Tritium Measurements". In: *Radiochemistry* 63.2, pp. 221–226. DOI: 10.1134/S1066362221020120.

Baburajan, A. et al. (Mar. 2020). "Tissue Free Water Tritium (TFWT) and Organically Bound Tritium (OBT) in Marine Eco System at Tarapur on the West Coast of India". In: *Journal of Radioanalytical and Nuclear Chemistry* 323.3, pp. 1431–1441. DOI: 10.1007/s10967-019-06861-7.

Baglan, N., C. Cossonnet, et al. (Jan. 2018). "Feedback of the Third Interlaboratory Exercise Organised on Wheat in the Framework of the OBT Working Group". In: *Journal of Environmental Radioactivity* 181, pp. 52–61. DOI: 10.1016/j.jenvrad.2017.09.009.

Baglan, N., S.B. Kim, et al. (Jan. 2013). "Organically Bound Tritium (OBT) Behaviour and Analysis: Outcomes of the Seminar Held in Balaruc-les-Bains in May 2012". In: *Radioprotection* 48.1, pp. 127–144. DOI: 10.1051/radiopro/2012051.

Balina, Karina, Francesco Romagnoli, and Dagnija Blumberga (Sept. 2016). "Chemical Composition and Potential Use of Fucus Vesiculosus from Gulf of Riga". In: *Energy Procedia* 95, pp. 43–49. DOI: 10.1016/j.egypro.2016.09.010.

Belot, Yves, Monique Roy, and Henri Métivier (1997). *Le tritium: de l'environnement à l'homme*. Les Ulis: les Éd. de Physique.

Birks, J B (Oct. 1951). "Scintillations from Organic Crystals: Specific Fluorescence and Relative Response to Different Radiations". In: *Proceedings of the Physical Society. Section A* 64.10, pp. 874–877. DOI: 10.1088/0370-1298/64/10/303.

Broda, Ryszard, Philippe Cassette, and Karsten Kossert (Aug. 2007). "Radionuclide Metrology Using Liquid Scintillation Counting". In: *Metrologia* 44.4, S36–S52. DOI: 10.1088/0026-1394/44/4/S06.

Carles, Grau et al. (Feb. 2004). "Ionization Quenching in LSC". In: *Applied Radiation and Isotopes* 60.2–4, pp. 447–451. DOI: 10.1016/j.apradiso.2003.11.057.

Chen, Qianyuan et al. (June 2022a). "Verification of Combustion Rate of Recovery and Counting Efficiency in the Analysis of Organically Bound Tritium in Biota Samples". In: *Applied Radiation and Isotopes* 184, p. 110202. DOI: 10.1016/j.apradiso.2022.110202.

— (June 2022b). "Verification of Combustion Rate of Recovery and Counting Efficiency in the Analysis of Organically Bound Tritium in Biota Samples". In: *Applied Radiation and Isotopes* 184, p. 110202. DOI: 10.1016/j.apradiso.2022.110202.

Croudace, I. W., P. E. Warwick, and R. Marsh (Apr. 2017). "A Suite of Robust Radioanalytical Techniques for the Determination of Tritium and Other Volatile Radionuclides in Decommissioning Wastes and Environmental Matrices". In: *Fusion Science and Technology* 71.3, pp. 290–295. DOI: 10.1080/15361055.2017.1293450.

Crozet, Marielle et al. (May 2025). "First Wheat Certified Reference Material for Organically Bound Tritium Measurement in the Environment". In: *Talanta* 286, p. 127515. DOI: 10.1016/j.talanta.2025.127515.

Currie, Lloyd A. (Mar. 1968). "Limits for Qualitative Detection and Quantitative Determination. Application to Radiochemistry". In: *Analytical Chemistry* 40.3, pp. 586–593. DOI: 10.1021/ac60259a007.

Eyrolle, Frédérique et al. (Jan. 2018). "An Updated Review on Tritium in the Environment". In: *Journal of Environmental Radioactivity* 181, pp. 128–137. DOI: 10.1016/j.jenvrad.2017.11.001.

Farrow, F. et al. (May 2017). "Characteristics of the Combustion Water of Organically Bound Tritium (OBT) Measurements of Fish Samples". In: *Journal of Radioanalytical and Nuclear Chemistry* 312.2, pp. 433–441. DOI: 10.1007/s10967-017-5218-x.

Herforth, Lieselott and Hartmut Kallmann (Jan. 1949). "Die Fluoreszenzanregung von Festem Und Flüssigem Naphthalin, Diphenyl Und Phenanthren Durch Alphateilchen, Schnelle Elektronen Und Gammastrahlen. (Mit 11 Abbildungen)". In: *Annalen der Physik* 439.5, pp. 231–245. DOI: 10.1002/andp.19494390503.

Hidex Oy (2023). *Hidex 300 SL Automatic TDCR Liquid Scintillation Counter: Technical Specifications*. Turku, Finland: Hidex Oy.

Hunt, G J et al. (Mar. 1, 2010). "Enhancement of Tritium Concentrations on Uptake by Marine Biota: Experience from UK Coastal Waters". In: *Journal of Radiological Protection* 30.1, pp. 73–83. DOI: 10.1088/0952-4746/30/1/N01.

IAEA (Mar. 2025). *Tritium in the Environment*. Technical Reports Series. INTERNATIONAL ATOMIC ENERGY AGENCY. DOI: 10.61092/iaea.0qjt-xo5o.

ICRP (1990). "Age-Dependent Doses to Members of the Public from Intake of Radionuclides. 1". In: 1. ed. ICRP Publication Radiation Protection 56. Oxford: Pergamon Press.

Jakonić, Ivana et al. (May 2014). "Optimization of Low-Level LS Counter Quantulus 1220 for Tritium Determination in Water Samples". In: *Radiation Physics and Chemistry* 98, pp. 69–76. DOI: 10.1016/j.radphyschem.2014.01.012.

Kim, S. B. et al. (July 2008). "HTO and OBT Concentrations in a Wetland Ecosystem". In: *Fusion Science and Technology* 54.1, pp. 248–252. DOI: 10.13182/FST08-A1805.

Kim, S.B. and V. Korolevych (Apr. 2013). "Quantification of Exchangeable and Non-Exchangeable Organically Bound Tritium (OBT) in Vegetation". In: *Journal of Environmental Radioactivity* 118, pp. 9–14. DOI: 10.1016/j.jenvrad.2012.11.006.

Krištof, Romana, Natasha Chipanovska, and Jasmina Kožar Logar (May 2023). "Determining the Amounts of Organically Bound Tritium and Radiocarbon Using a Combined Preparation Step and Liquid Scintillation Spectrometry". In: *Journal of Radioanalytical and Nuclear Chemistry* 332.5, pp. 1521–1526. DOI: 10.1007/s10967-022-08586-6.

Kuwata, Haruka et al. (May 2025). "Optimization and Validation of Combustion-Based Analysis of Organically Bound Tritium in Pine Needles". In: *Journal of Radioanalytical and Nuclear Chemistry* 334.5, pp. 3185–3192. DOI: 10.1007/s10967-025-10063-9.

L'Annunziata, Michael F. and Michael J. Kessler (2012). "Liquid Scintillation Analysis". In: *Handbook of Radioactivity Analysis*. Elsevier, pp. 423–573. DOI: 10.1016/B978-0-12-384873-4.00007-4.

Lecompte, Yannick et al. (June 2020). "TRITIUM ANALYSIS IN URINE BY THE TRIPLE-TO-DOUBLE COINCIDENCE RATIO METHOD WITH THE HIDEX 300 SL LIQUID SCINTILLATION COUNTER". In: *Radiation Protection Dosimetry* 188.2, pp. 148–161. DOI: 10.1093/rpd/ncz270.

Lin, Feng et al. (Jan. 2020). "A Method for the Determination of Organically Bound Tritium in Marine Biota Based on an Improved Tubular-Combustion System". In: *Journal of Environmental Radioactivity* 211, p. 106084. DOI: 10.1016/j.jenvrad.2019.106084.

Love, Adam H., James R. Hunt, and John P. Knezovich (Oct. 1, 2003). "Reconstructing Tritium Exposure Using Tree Rings at Lawrence Berkeley National Laboratory, California". In: *Environmental Science & Technology* 37.19, pp. 4330–4335. DOI: 10.1021/es034278d.

Nayak, S. Rashmi et al. (Mar. 2019). "Organically Bound Tritium: Optimization of Measurements in Environmental Matrices by Combustion Method and Liquid Scintillation Spectrometry". In: *Journal of Radioanalytical and Nuclear Chemistry* 319.3, pp. 917–926. DOI: 10.1007/s10967-018-6395-y.

NPL (2006). *1220 QUANTULUS: 1220-307 WinQ, Quantulus User Interface*. National Physical Laboratory.

Ohki, Mayu et al. (Sept. 2021). "Working Environment of Tritium Analysis for Photoluminescence Control". In: *Fusion Engineering and Design* 170, p. 112679. DOI: 10.1016/j.fusengdes.2021.112679.

Paquet, F. et al. (Dec. 2016). "ICRP Publication 134: Occupational Intakes of Radionuclides: Part 2". In: *Annals of the ICRP* 45.3–4, pp. 7–349. DOI: 10.1177/0146645316670045.

Pédehontaa-Hiaa, G. et al. (Mar. 2020). "Tritium in Urine from Members of the General Public and Occupationally Exposed Workers in Lund, Sweden, Prior to Operation of the European Spallation Source". In: *Journal of Environmental Radioactivity* 213, p. 106141. DOI: 10.1016/j.jenvrad.2019.106141.

Pointurier, F, N Baglan, and G Alanic (Aug. 2004). "A Method for the Determination of Low-Level Organic-Bound Tritium Activities in Environmental Samples". In: *Applied Radiation and Isotopes* 61.2–3, pp. 293–298. DOI: 10.1016/j.apradiso.2004.03.024.

Pointurier, F. et al. (Jan. 2003). "Determination of Organically Bound Tritium Background Level in Biological Samples from a Wide Area in the South-West of France". In: *Journal of Environmental Radioactivity* 68.2, pp. 171–189. DOI: 10.1016/S0265-931X(03)00053-5.

PROCORAD (2025). *INTERLABORATORY COMPARISON CAMPAIGN PLAN 2026*. Association pour la Promotion du Contrôle de Qualité des Analyses de Biologie Médicale en Radiotoxicologie.

Pujol, \ relax Ll. and J. A. Sanchez-Cabeza (Nov. 1999). "Optimisation of Liquid Scintillation Counting Conditions for Rapid Tritium Determination in Aqueous Samples". In: *Journal of Radioanalytical and Nuclear Chemistry* 242.2, pp. 391–398. DOI: 10.1007/BF02345568.

Raddec International (2024). *DATA SHEET: Pyrolyser-6 Trio GenIV Furnace System*.

Ross, A et al. (Sept. 2008). "Classification of Macroalgae as Fuel and Its Thermochemical Behaviour". In: *Bioresource Technology* 99.14, pp. 6494–6504. DOI: 10.1016/j.biortech.2007.11.036.

Schäfer, I, D Hebert, and U Zeiske (July 2000). "On Low-Level Tritium Measurements with LSC Quantulus". In: *Applied Radiation and Isotopes* 53.1–2, pp. 309–315. DOI: 10.1016/S0969-8043(00)00146-9.

Schubert, Florian and Jens Kallmeyer (July 2023). "Liquid Scintillation Counting at the Limit of Detection in Biogeosciences". In: *Frontiers in Microbiology* 14, p. 1194848. DOI: 10.3389/fmicb.2023.1194848.

Song, You-xue et al. (2016). "Parameters Optimization of Hidex 300SL Liquid Scintillation Counter for Measuring Activity of Low-Level Tritium Water". In: *Nuclear Techniques* 38.1, p. 010043. DOI: 10.7538/hhx.2016.38.01.0043.

*Standard Methods FOR THE Examination of Water and Wastewater 20th Edition* (1998).

University of Saskatchewan (n.d.). *Tri-Carb 2810TR Low Activity Liquid Scintillation Analyzer*. University of Saskatchewan.

Varlam, C. et al. (May 2009). "Applying Direct Liquid Scintillation Counting to Low Level Tritium Measurement". In: *Applied Radiation and Isotopes* 67.5, pp. 812–816. DOI: 10.1016/j.apradiso.2009.01.023.

World Health Organization, ed. (2017). *Guidelines for Drinking-Water Quality*. Fourth edition incorporating the first addendum. Geneva: World Health Organization. 1 p.

Yang, Guosheng et al. (Apr. 29, 2026). "Intercomparison of Tritium Analysis in Urine and Water". In: *Journal of Radioanalytical and Nuclear Chemistry*. DOI: 10.1007/s10967-026-10912-1.

Zaharov, Simona (2025). "QUANTIFYING THE ORGANICALLY-BOUND TRITIUM LEVELS IN THE ENVIRONMENTAL SAMPLES AROUND THE CERNAVODA NUCLEAR POWER PLANT". In: *Sci. Bull* 87.2.

Zaharov, Simona, A.E. Nedelcu, and D. Dupleac (July 2025). "Evaluation of the Sample Preparation Method for Environmental Reference Matrices Suitable for Organically-Bound Tritium Interlaboratory Comparison Exercises". In: *Journal of Environmental Radioactivity* 287, p. 107730. DOI: 10.1016/j.jenvrad.2025.107730.

# Background A
# Theoretical TDCR

This appendix provides the mathematical derivation for the theoretical TDCR model and its application to efficiency corrections. While this specific analytical approach was not the primary method used for the TDCR corrections in this thesis, the underlying physics remains identical. A formal derivation of the model promotes a deeper understanding of the relationship between ionization quenching and detection efficiency that dictates all TDCR-based methodologies.

## A.1 Derivation

The theoretical detection efficiencies are determined by modeling the probability of generating photoelectrons in the PMTs using Poisson statistics. A PMT produces a discrete number of photoelectrons. The probability of producing k photoelectrons given an average of m is described by the Poisson distribution:

$$P(m,k) = \frac{e^{-m}m^k}{k!} \tag{A.1}$$

Where $P(m,k)$ is the probability of producing $k$ photoelectrons given an average of $m$. In the free-parameter model $m$ is defined as:

$$m = \frac{E \cdot Q(E)}{3\lambda} \tag{A.2}$$

Where E is the energy of the $\beta$ particle, $\lambda$ is the average energy needed to produce a single photoelectron. $\lambda$ is intrinsic to the LSC system (Broda, Cassette, and Kossert 2007). The factor 3 accounts for the 3 PMT's sharing the production of photoelectrons.
The ionization quenching correction $Q(E)$ corrects for scintillation light loses as described in Section 2.3.3.1. It is described by Birks law (Birks 1951):

$$Q(E) = \frac{1}{E}\int_0^E \frac{dE}{1 + k_B \cdot \frac{dE}{dx}} \tag{A.3}$$

Where $k_B \cdot \frac{dE}{dx}$ represents the quenching loss over the path length of the $\beta$ particle, and $k_B$ is Birk's coefficient.
Using these single-PMT probabilities, the detection probabilities for a triple-PMT system are computed next. The probability of detecting at least one photon in a PMT is given by:

$$P(m, k \geq 1) = 1 - e^{-m} \tag{A.4}$$

The probabilities of detecting double and triple coincidences are found by simple combinatorial analysis. Note that the double coincidence probability includes events where all three PMTs register a photon. Assuming identical PMTs, the probabilities are:

$$P_{double} = 3(1-e^{-m})^2 - 2(1-e^{-m})^3 \quad P_{triple} = (1-e^{-m})^3 \tag{A.5}$$

The theoretical value for the total triple and double counts detected over a selected ROI is found by integrating over the samples decay profile S(E) along with the respective detection probability distributions:

$$N\epsilon_{double} = \int_{E_{low}}^{E_{max}} P_{double}(E) \cdot S(E)dE \quad N\epsilon_{triple} = \int_{E_{low}}^{E_{max}} P_{triple}(E) \cdot S(E)dE \tag{A.6}$$

Where N is the total number of disintegrations occurring in the sample during the measurement period. The theoretical TDCR value is then:

$$TDCR = \frac{\epsilon_{triple}}{\epsilon_{double}} = \frac{\int_{E_{low}}^{E_{max}} P_{triple}(E) \cdot S(E)dE}{\int_{E_{low}}^{E_{max}} P_{double}(E) \cdot S(E)dE} \tag{A.7}$$

## A.2 Application

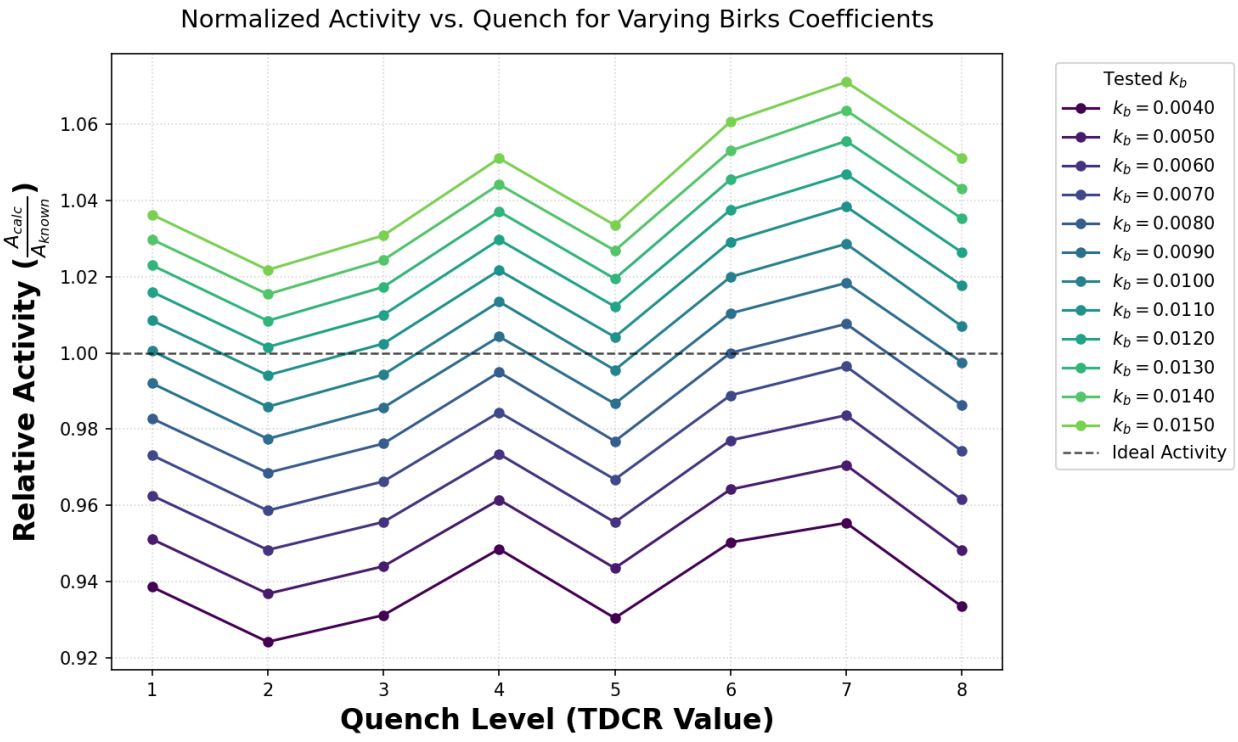


Figure A.1: Plot of relative activity for standard of equal activity with varying quench levels. Each separate line represents a different tested Birks coefficient. Since, no line is flat none of the coefficients are acceptable.

Numerical approaches will have a theoretical beta decay spectra for the specific scintillation cocktail used. $k_b$ is a parameter that determines the strength of the ionization quench. The ionization quench is intrinsic and therefore does not change when adding quenching agents such as nitromethane (Arun, Viswanathan, et al. 2021). Birks coefficient is determined by preparing multiple identical standard samples with known activity and different quench levels. Ionization quench remains constant while the color and chemical quench are controlled by the quantity of the quenching agent applied. Several Birks coefficients are tested and the TDCR vs the activity is plotted for each factor tested. The Birks coefficient is taken as the tested coefficient that gives the most constant activities over the quench range (Lecompte et al. 2020), due to ionization quench levels not changing. An example of such a plot is shown in Figure A.1, however in the case shown none of the factors were suitable. With $\lambda$ being the only unknown parameter, it will be numerically fitted to the theoretical spectra and accurate efficiencies are then returned.

In summary, the theoretical approaches measure the TDCR value of the sample experimentally, analytically determining $k_b$, and then iteratively varying the free parameter $\lambda$ until the theoretical TDCR matches the measured value (L'Annunziata and Kessler 2012, Arun, Viswanathan, et al. 2021).

# Background B
# Simulation Data

This appendix provides the full set of simulated standard deviation used to calculate the sign-test statistics as discussed in Section 4.3.1

Table B.1: Simulated standard deviations of the sign-test statistic for different batch sizes.

| **N** | $\sigma$ | **N** | $\sigma$ | **N** | $\sigma$ | **N** | $\sigma$ |
|---|---|---|---|---|---|---|---|
| 2 | 0.99999995 | 26 | 3.00056232 | 50 | 4.12231940 | 74 | 5.00171010 |
| 3 | 1.15491896 | 27 | 3.05450320 | 51 | 4.16121028 | 75 | 5.03441853 |
| 4 | 1.29070820 | 28 | 3.11133389 | 52 | 4.19907514 | 76 | 5.06722311 |
| 5 | 1.41394752 | 29 | 3.16470202 | 53 | 4.24276438 | 77 | 5.09984092 |
| 6 | 1.52883223 | 30 | 3.21461077 | 54 | 4.28251048 | 78 | 5.12944635 |
| 7 | 1.63388132 | 31 | 3.26526191 | 55 | 4.31985713 | 79 | 5.16163562 |
| 8 | 1.73222053 | 32 | 3.31994756 | 56 | 4.36108243 | 80 | 5.19590174 |
| 9 | 1.82604491 | 33 | 3.36604690 | 57 | 4.39526500 | 81 | 5.22641751 |
| 10 | 1.91434062 | 34 | 3.41757723 | 58 | 4.43330051 | 82 | 5.25974332 |
| 11 | 2.00134450 | 35 | 3.46324910 | 59 | 4.47342948 | 83 | 5.29148337 |
| 12 | 2.08183245 | 36 | 3.50856934 | 60 | 4.50784554 | 84 | 5.32466974 |
| 13 | 2.16056390 | 37 | 3.55776215 | 61 | 4.55153465 | 85 | 5.34880378 |
| 14 | 2.23452722 | 38 | 3.60433124 | 62 | 4.58199929 | 86 | 5.38566136 |
| 15 | 2.30890808 | 39 | 3.65214169 | 63 | 4.62128039 | 87 | 5.41499838 |
| 16 | 2.38005428 | 40 | 3.69907968 | 64 | 4.65411412 | 88 | 5.44639374 |
| 17 | 2.44978384 | 41 | 3.74063687 | 65 | 4.68751954 | 89 | 5.48187921 |
| 18 | 2.51675661 | 42 | 3.78433421 | 66 | 4.72974515 | 90 | 5.50477928 |
| 19 | 2.58405684 | 43 | 3.82898341 | 67 | 4.76567703 | 91 | 5.53308142 |
| 20 | 2.64583879 | 44 | 3.87320062 | 68 | 4.79804727 | 92 | 5.57089022 |
| 21 | 2.70982545 | 45 | 3.91688662 | 69 | 4.82812599 | 93 | 5.59600047 |
| 22 | 2.76803961 | 46 | 3.95826674 | 70 | 4.86308507 | 94 | 5.62268863 |
| 23 | 2.82555564 | 47 | 4.00081809 | 71 | 4.90020331 | 95 | 5.65565030 |
| 24 | 2.88852433 | 48 | 4.04036004 | 72 | 4.93626660 | 96 | 5.68927657 |
| 25 | 2.94639911 | 49 | 4.08399352 | 73 | 4.96499325 | 97 | 5.71720380 |

# Background C
# LSC Application UI images

The following figures illustrate the software implementation developed for this study using the PySide 6 framework. The application was designed to provide a cohesive workflow between raw data acquisition and final quantification. The gallery below demonstrates the three primary operational modes: the Home Interface, the Data Processing Table, and the Spectra Visualization module.

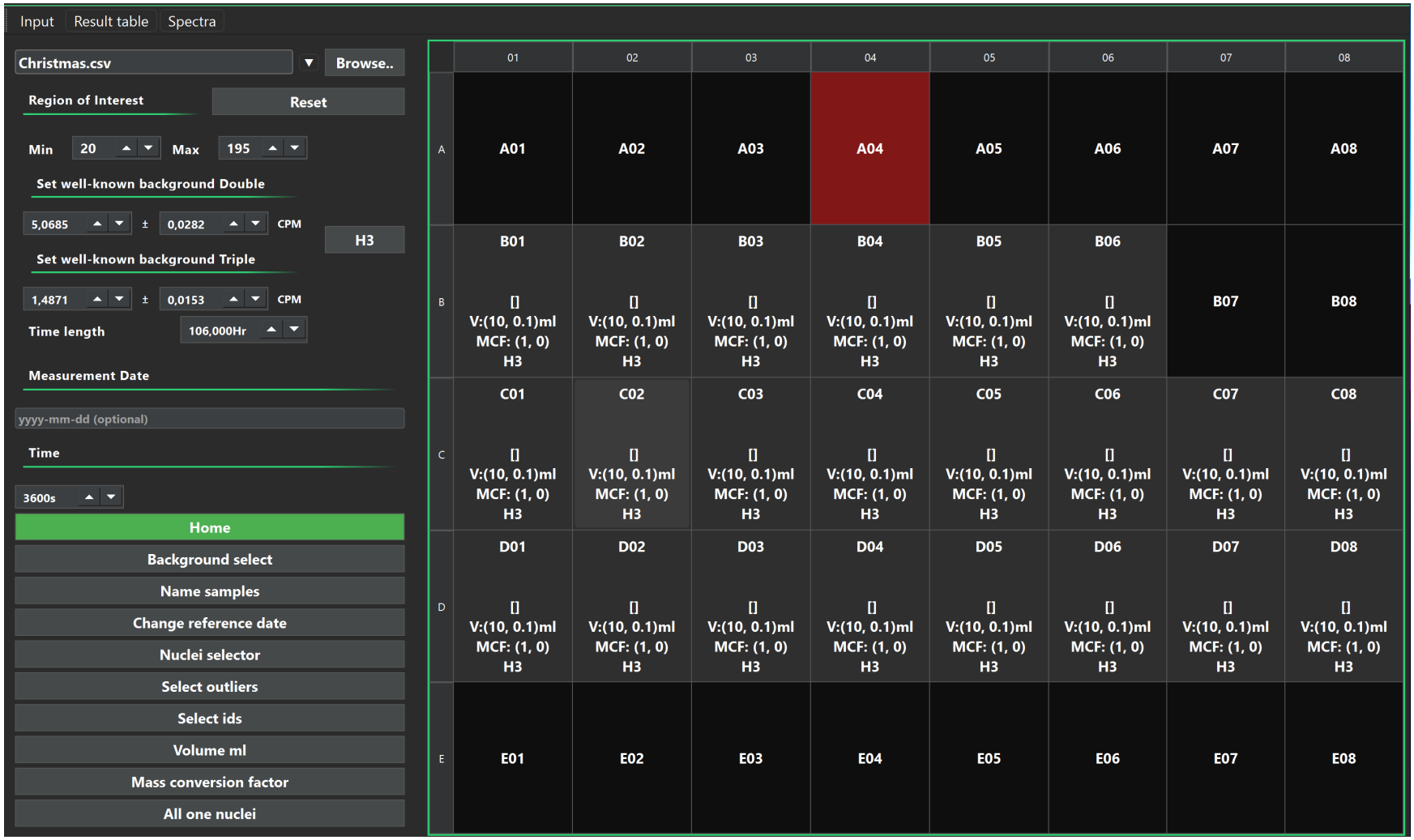


Figure C.1: Home window of the application. The measurement tray is visualized to the right. Red cells correspond to the blank.

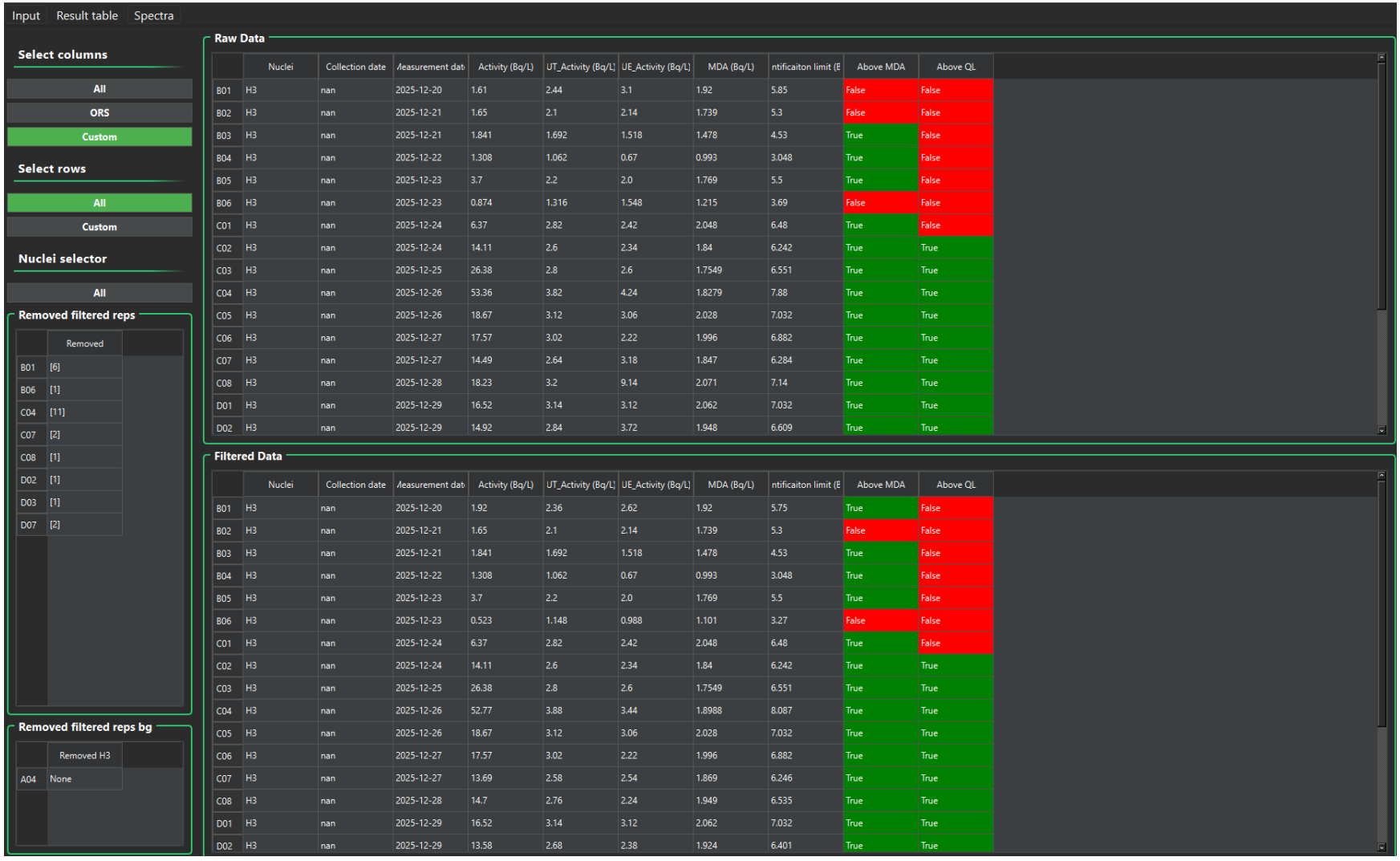


Figure C.2: Data table view window of application. Green and red cells indicate if the activity is above the MDA and the AQL. **Top right:** Raw data (No reps removed). **Bottom right:** Data filtered according to the cleaning process. **Middle left:** Repetitions removed from samples. **Bottom left:** Repetitions removed from Background.

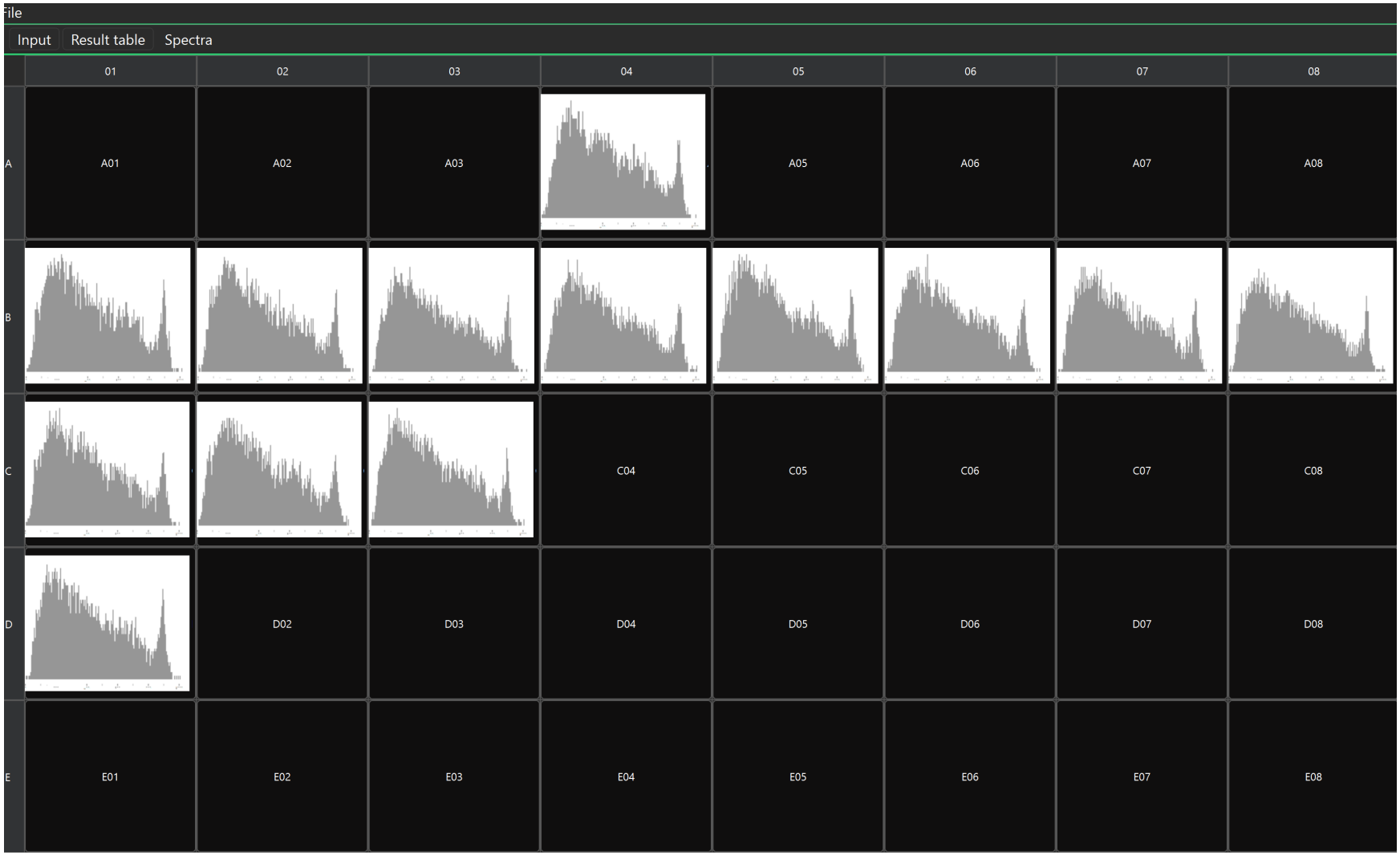


Figure C.3: Image of the spectra viewer section of the application. Each graph is a button that opens further graph views for the specified sample.